Brigham Young University
BYU ScholarsArchive

All Theses and Dissertations

2017-12-01

The Morphology and Uniformity of Circumstellar OH/H_2O Masers around OH/IR Stars

Derek Sean Felli
Brigham Young University

Follow this and additional works at: https://scholarsarchive.byu.edu/etd

Part of the Astrophysics and Astronomy Commons

BYU ScholarsArchive Citation

Felli, Derek Sean, "The Morphology and Uniformity of Circumstellar OH/H_2O Masers around OH/IR Stars" (2017). *All Theses and Dissertations*. 6633.
https://scholarsarchive.byu.edu/etd/6633

This Dissertation is brought to you for free and open access by BYU ScholarsArchive. It has been accepted for inclusion in All Theses and Dissertations by an authorized administrator of BYU ScholarsArchive. For more information, please contact scholarsarchive@byu.edu, ellen_amatangelo@byu.edu.

The Morphology and Uniformity of

Circumstellar OH/H_2O Masers

Around OH/IR Stars

Derek Sean Felli

A dissertation submitted to the faculty of
Brigham Young University
in partial fulfillment of the requirements for the degree of

Doctor of Philosophy

Victor Migenes, Chair
Denise C. Stephens
Eric G. Hintz
J. Ward Moody
Clark G. Christensen

Department of Physics and Astronomy

Brigham Young University

Copyright © 2017 Derek Sean Felli

All Rights Reserved

ABSTRACT

The Morphology and Uniformity of
Circumstellar OH/H_2O Masers
Around OH/IR Stars

Derek Sean Felli
Department of Physics and Astronomy, BYU
Doctor of Philosophy

Even though low mass stars (< 8 solar masses) vastly outnumber high mass stars (> 8 solar masses), the more massive stars drive the chemical evolution of galaxies from which the next generation of stars and planets can form. Understanding mass loss of asymptotic giant branch stars contributes to our understanding of the chemical evolution of the galaxy, stellar populations, and star formation history. Stars with mass < 8 solar masses form planetary nebulae, while those with mass > 8 solar masses go supernova. In both cases, these stars enrich their environments with elements heavier than simple hydrogen and helium molecules. While some general info about how stars die and form planetary nebulae are known, specific details are missing due to a lack of high-resolution observations and analysis of the intermediate stages. For example, we know that mass loss in stars creates morphologically diverse planetary nebulae, but we do not know the uniformity of these processes, and therefore lack detailed models to better predict how spherically symmetric stars form asymmetric nebulae. We have selected a specific group of late-stage stars and observed them at different scales to reveal the uniformity of mass loss through different layers close to the star. This includes observing nearby masers that trace the molecular shell structure around these stars. This study revealed detailed structure that was analyzed for uniformity to place constraints on how the mass loss processes behave in models. These results will feed into our ability to create more detailed models to better predict the chemical evolution of the next generation of stars and planets.

Keywords: radio, OH/IR, astronomy, maser, star, planetary nebulae, mass loss

ACKNOWLEDGMENTS

I'd like to thank each member of my committee for the trust they placed in me to finish this work. Dr. Stephens took on teaching an extra course and provided valuable feedback. Dr. Moody allowed me to work with my chosen advisor, Dr. Migenes, and showed great interest when I developed my own techniques for my data analysis. Dr. Hintz provided help and shared his expertise on stellar life cycles. Dr. Christensen provided valuable insights in checking that my facts were sound.

Thank you to Dr. Joner, who spent time taking data at West Mountain so that we could test to see if our telescope could detect the dusty environments around the stars I studied.

My graduate colleagues and fellow radio astronomers Adam Johanson and Brandon Wiggins were a great moral support and inspiration to me when we spent time in the office. I am the last to finish among them and remember great unity and support among us.

My wife Melissa was a great source of pushing this work to be completed. She helped with organizing all the content I could verbally explain and helped draft and edit large sections of the dissertation. Her feedback was timely and she helped tremendously. Your name almost replaces mine on the dissertation. Thank you.

My advisor, Dr. Victor Migenes, was a real trooper in taking me on as a graduate student. He placed a lot of trust in me. The later circumstances were such that he was away at an out of state university while I was finishing up off campus. That threw a lot of the responsibility on me, but Victor made time when I needed direction on how to progress with the data analysis. His encouragement motivated me. Thank you for that trust, you are a great mentor.

Contents

Chapter 1

Introduction

Objects in space evolve along currents of matter that lace the universe in patterns somewhat similar to the weather patterns that are observed on earth. Like weather, these patterns are influenced by temperature and pressure, but instead of forming storms, heavy rain or fierce updrafts, this matter is what creates stars, planets, supernova remnants, and planetary nebulae of all sizes. Low mass stars vastly outnumber stars with a high mass, but it is these stars with higher masses that are more critical to forming diverse planets and contribute to the evolution of our 'galactic climate'. It is only during the late stages of an intermediate or high mass star's life that a star begins fusing the heavier elements like carbon, nitrogen, oxygen, nickel, and iron–the building blocks of life and of planets. As these stars evolve, these heavier materials are dispersed into regions surrounding the star and are scattered throughout space. High mass stars (> 8 $M_\odot$) can go supernova, flinging heavier elements great distances and producing even heavier elements in the explosion. Intermediate and low mass stars (< 8 $M_\odot$) at the time of their death form into planetary nebulae and push these heavy elements into their surroundings at speeds of 7-30 km/s. They typically lose mass at rates of 10^{-6} to an incredible 10^{-4} $M_\odot$/year (te Lintel Hekkert et al. 1991). Understanding these types of stars in their late stage of evolution is the crux of understanding current galactic chemistry and where it is headed.

Mass plays an important role in determining the stages a star goes through and is the strongest indicator of how a star will evolve and eventually die. We also note that a star's chemical composition, like being richer in heavier metals, plays an important role in a star's evolution by providing alternate paths to radiate energy. Even though a star's initial mass and composition are good indicators of what a star's life will be, the mass loss processes that more readily affect medium to larger stars may drastically affect the important end stages of a star.

We know that stars of specific masses (2-10 $M_\odot$) are extremely prone to high mass loss, so we have chosen these to study their evolution and the role they play in the recycling medium of the galaxy.

1.1 The Life Cycle of Stars

In order to understand the pivotal role that stars play in the chemical makeup of the interstellar medium, it is necessary to first understand the life cycle of a star and the various paths that it can take in its evolution. Stars begin their lives in giant molecular clouds and gas nebulae, form protostars, become main sequence stars, ripen into giant and supergiant stars, and die either by going supernova or becoming planetary nebulae. Special circumstances can produce certain types of stars, such as OH/IR stars, that form in this late stage and provide unique opportunities to study the dying processes, mass loss, and the seeding of matter throughout nearby space.

“Nebulas are key players in the birth of stars. The incubation process begins with the contraction of dark globules within the nebula. Globules contract until they collapse under the force of their own gravity, precipitating the birth of stars.” (Baumann et al. 2007). Nebulae have the potential for hundreds and sometimes thousands of stars to develop inside their dusty veils. When globules of matter contract together due to gravity, they become denser and produce massive amounts of heat. This collapsing globule is known as a protostar. The protostar is spinning, conserving the original angular momentum of the infalling material. The gravitationally drawn material will also spin, causing it to flatten and form into a dusty disk. This happens because material outside the plane of rotation has a component of gravitational force always toward the plane of rotation and a centripetal component toward the spin axis. Since the material is in-falling and spinning, the force toward the spin axis will mainly hold the material in a circle, and the force toward the rotation plane accelerates material toward that plane to form the disk. This material can lose energy through friction and spiral inward to feed the growth of the protostar. Eventually, the continued compression of mass deep inside of the protostar will generate additional heat until it reaches a high enough temperature to trigger a nuclear reaction and balance out the contraction, starting fusion within the newly formed star.

1.1.1 The main sequence stars

After the brief protostar phase lasting 10^4 - 10^7 years (high mass stars), the now stable star fuses hydrogen into helium and is a main sequence star. This constitutes the longest phase in a star's lifespan. This fusion creates energy that is radiated away, creating a pressure gradient equal to the inward gravitational force. These main sequence stars lie in a well-defined area on an absolute luminosity vs temperature plot (referring to an H-R diagram) (see Fig. 1.1). In simplest terms, mass determines destiny. The stellar mass also determines temperature, luminosity (brightness), lifespan, and color. The rule of thumb for main sequence stars is that higher mass stars are bluer, brighter, hotter, and larger. Cooler stars are less luminous and less massive, smaller, and are redder in color. Hotter stars "burn" faster (1-100 million years), therefore consuming the hydrogen in their cores faster and beginning their evolved giant phases sooner. Cooler, redder stars usually live longer (100 million years to longer than 10 billion years) because they "burn" slower. These timescales make the presence of nearby intermediate to high mass stars a very rare find, but taking advantage of the ones present provides an important opportunity to learn more about how the mass loss process works among these stars in an uncommon short-lived stage.

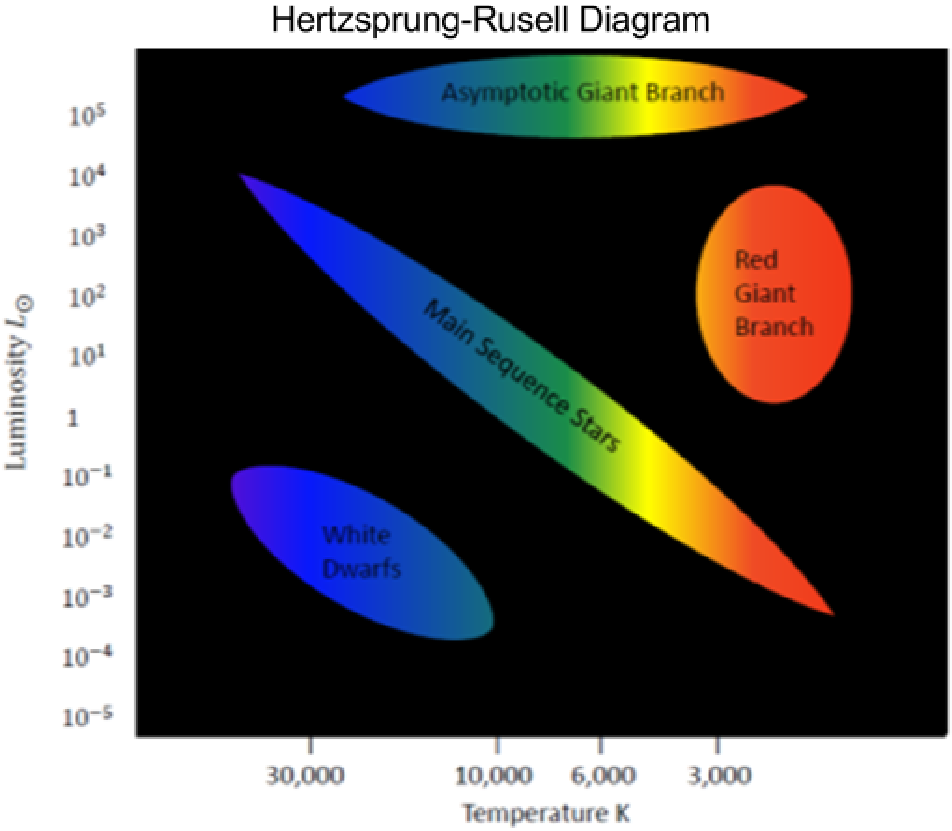

Figure 1.1 Hertzsprung-Russell Diagram absolute luminosity (solar lumins) vs temperature (K). Stars that fall into different areas on this diagram are classified accordingly.

Main sequence stars continue to fuse hydrogen for most of their lives. Eventually, however, the hydrogen that fuels fusion begins to run out. Once there is no longer enough hydrogen in the core for fusion to occur, the star begins to collapse under the force of gravity. At this point, the star leaves the main sequence and can start down several fascinating roads depending on the star's mass. The stars over 0.6 $M_{\odot}$ will go through the following phases: red giant phase, a horizontal branch stage, and an asymptotic branch stage. Asymptotic giant branch stars are of particular importance to this study because they exhibit high mass loss which can drastically change the entire process of the star's death.

1.1.2 Red Giant Branch

When all the hydrogen in the core is used up, the radiative pressure from fusion no longer fully counteracts the gravitational pull, so the core compresses further and further and heats up. At this stage convection zones can dredge up materials from inner layers, even as far down as the core, bringing fused materials such as helium to the surface. This particular dredge-up process is known as the first dredge-up. This changes the composition of the outer surface of a star. When combined with mass loss processes, these materials are carried away from the surface of the star to enrich its circumstellar envelope with heavier elements. Later periods of dredge-up include the second and third dredge-up, although not all stars will experience every dredge-up process. These later dredge-up processes will bring even heavier elements to the surface than the first.

Hydrogen fusion starts to take place outside the core in a shell, producing larger amounts of heat and pressure than that which was present when the core was fusing hydrogen. During shell fusion, the core begins to heat past the point needed for hydrogen fusion. This additional heat causes the outer layers of the star to expand in a direct contrast to its shrinking core. The star's core heats up during this collapse and becomes extremely dense. When the core becomes one-tenth its former size, it reaches a high enough temperature to fuse helium (Baumann et al. 2007).

During the Red Giant Branch stage, stars around 1 - 2 $M_\odot$ become very compact in their core and become degenerate before the onset of helium fusion. This means that the material in the core has collapsed so closely together by extremely high pressures that it has reached the physical limits of those materials and can no longer be compressed into a smaller space. These stars increase in temperature until conditions are ripe for helium fusion. At this stage, these stars undergo an explosive fusion of helium (called the helium flash) that releases an enormous amount of energy to lift the degeneracy. Stars more massive than 2 $M_\odot$ start helium fusion before the core can become degenerate and do not incur a helium flash.

1.1.3 Horizontal branch

When a star starts helium fusion in its core, a star reaches the horizontal branch stage. Hydrogen shell fusion is actually able to take place outside the core, inside one of the outer shells, and deposits its product (helium) down into the outer layers of the core. This stage is characterized by small luminosity changes and increasing temperature.

1.1.4 Asymptotic Giant Branch

Asymptotic Giant Branch stars form from low to intermediate mass stars (0.8-10 $M_\odot$). These stars become enormous, sometimes as wide across as 1700 solar radii. As an asymptotic star matures, the shell fusion occurs through multiple layers (like hydrogen, helium, and carbon) which leads to instabilities in the star's structure. They pulsate on the order of 100 - 2000 days (Herman et al. 1985). Typically these stars periodically undergo hydrogen and helium fusion in their outer layers or shells. This causes the luminosity and size of the star to fluctuate fairly drastically.

When fusion occurs in shells it can occur unevenly or in pockets with convection transferring energy and material. Shell fusion products typically feed the next inner layer. Either the inner fusion shell moves outward to envelop the material or convection brings the material deeper into the star to be fused while concurrently mixing the star or dredging up heavy material to the stellar surface. Fusion rates differ, so some layers may burn all available material or become too hot to continue the fusion process. Increased temperature may also decrease fusion rates by increasing average particle speed, disallowing them sufficient interaction time to potentially fuse. These layers sit dormant for a while until some shift of structure or temperature ripens the conditions for fusion to start again. During ceased fusion, the internal structure starts to shrink until more fusion is induced to hold up or expand the star. This occurs in cycles and causes the star to pulsate over long periods of time ($\sim$1000 days).

On top of pulsations, thermal pulsations due to instabilities in the shell fusion, can occur. A thermal pulsation is a dramatic increase in nuclear burning rate. Because there are so many fusion processes that can activate and deactivate, layers can shift into certain temperature zones such that a large amount of material becomes available for fusion. The process of fusing releases energy that heats its surroundings and sometimes feeds directly back into driving fusion at a faster rate. This creates run-away fusion and shell material is burned up quickly, causing a surge of energy. This energy causes excess pressure causing the star to expand, increasing its luminosity. With the star's increased size, the upper layers have lower surface gravity and can be more readily detached as the thermal energy exits from the star. This can cause it to detach and expand continually away. These layers are enriched by the dredge-up process (convection reaching into the core) to become part of a cooling circumstellar envelope. This causes a huge amount of mass loss in these stars that most stars can only sustain for typically less than 10^4 to 10^5 years.

Asymptotic Giant Branch stars are able to branch into several types of stars: M-type (oxygen-rich), C-type (carbon-rich), and S-type (carbon abundance approaching oxygen abundance). An asymptotic giant branch star that is a variable is known as a 'mira' variable star. Mira stars are very luminous and are constantly expanding and contracting. A mira star's outer layers form extremely distended circumstellar envelopes that form non-uniform shapes.

These envelopes detach completely from the star and form the beginning pieces of a planetary nebula. When its outer layers form a planetary nebula, the core, a white dwarf, is the leftover remnant. Mira variable stars may be either carbon-rich if convection is shallow and not effective at bringing oxygen to the surface or oxygen-rich in the alternate scenario. If the oxygen-rich star forms, stellar wind can carry away material from the star's surface that cools to form dust and gaseous shells. Dust absorbs stellar radiation and re-emits it mainly in the infrared, shifting its spectral distribution. The excess oxygen combines to form H_2O and H_2O masers can form. When the H_2O molecules are dragged out to extreme distances by the stellar wind, the interstellar medium photon dissociates the H_2O molecules into H and OH ions. At there great distances OH masers can form in its circumstellar envelope. This would be classified as an OH/IR star.

1.1.5 OH/IR Stars

OH/IR stars are highly evolved asymptotic giant branch stars. Their spectral energy density profiles peak in the infrared due to dust obscuration and the nearby regions exhibit strong OH maser lines at 1612 MHz in the radio. The typical 1612 MHz radio spectrum for these stars is a double-peaked spectrum. The two peaks are believed to belong to the two extreme pieces of a spherical shell of material expanding at constant velocity (Bowers et al. 1983). The peaks are labeled as the red-shifted or blue-shifted peak referring to the direction of the Doppler shift from the central star along the line of sight to the observer; red is away from us, blue is toward us.

Circumstellar envelopes develop from the significant mass loss in these stars. Thermal pulsations and stellar winds of OH/IR stars cause high amounts of mass loss from the stellar surfaces ranging from 10^{-6} $M_{\odot}$/year to an incredible 10^{-4} $M_{\odot}$/year (te Lintel Hekkert et al. 1991). This material is pushed off the surface of the star and continually expands away into the surrounding regions, forming a circumstellar envelope (eventually becoming a planetary nebula). The material lost from the stars cools and forms different varieties of dust and gas (OH, H_2O, SiO).

OH/IR stars develop shells of dust grains and gas (see Fig. 1.2). The gaseous shells are comprised of OH, H_2O, and SiO molecules that form at different distances from the star (Vlemmings et al. 2002). SiO is in abundance near the star's atmosphere ($\sim 10^{13}$ cm). Farther out, there are H_2O and dust layers. Beyond the H_2O layer, there is an OH layer. The phenomenon is believed to stem from stellar winds dragging H_2O, the lighter material, more efficiently than

SiO, and so the H_2O shell is farther from the star ($\sim 10^{14}$ cm). The H_2O that is found at the furthest distances is dissociated to H and OH (OH referring to an ion throughout this work) by the interstellar medium UV photons. Next, stellar winds drag even lighter OH molecules to even greater distances ($\sim 10^{16}$ cm). The densest portions of these molecular shells can be detected in the radio through their maser emission (maser shells).

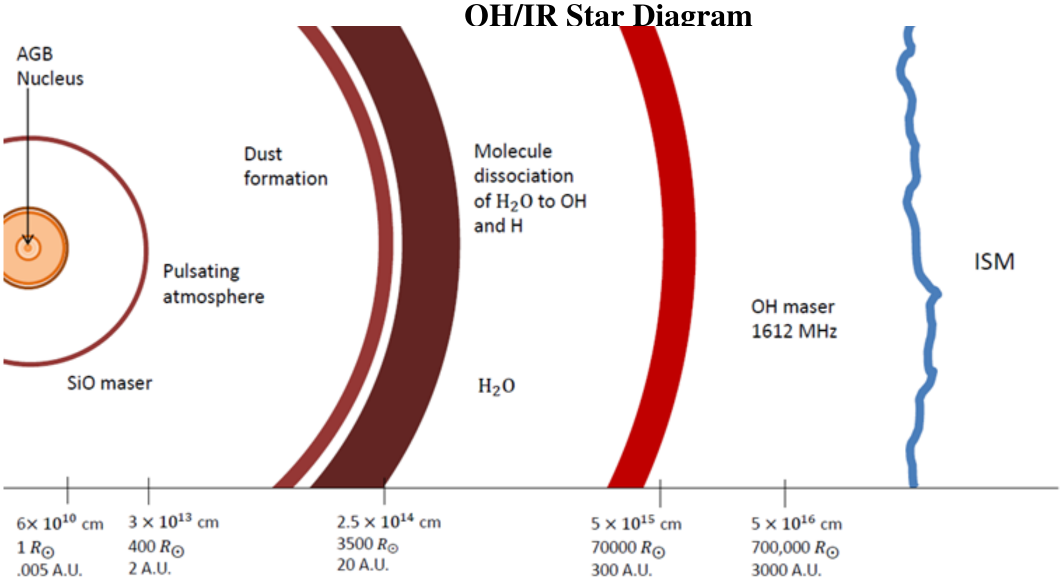

Figure 1.2 Simplified 2-D schematic of different shell layers and their approximate locations surrounding an OH/IR star.

The thickness of these maser shells relate to the thickness of the molecular shells (Netzer & Knapp 1987). OH maser shells have been observed and show non-uniformity, filaments, and gaps. (Migenes et al. 1991, Bowers et al. 1983). Conducting maser observations to learn about the sizes and shapes of the envelope can reveal how the mass-loss processes affect the evolution of these stars.

Distances to OH/IR stars have to be treated differently than that of main sequence stars. Main sequence stars have a well defined spectral type to luminosity relationship. This allows their distance to be calculated by relating their apparent brightness to their absolute brightest (derived from luminosity). Unlike main sequence stars, OH/IR stars don't have a well-defined method to determine luminosity. These stars are enshrouded in dust and highly obscured (high extinction). Direct measurement of their apparent luminosities is usually not possible in the visible spectrum. The sheer amount of dust has shifted the peak spectral energy distribution to the infrared. Other methods must come into play to determine distances to these objects.

Fortunately, other techniques have yielded distances of some candidates that are near enough to observe. The technique is to consistently monitor the spectral profiles of these stars and watch for variations. This technique is known as measuring the phase lag. Since these stars have a predominant OH maser line (1612 MHz) peaked at the red-shifted maser shell and blue-shifted maser shell, variations in one shell affect the other. For instance, a sudden increase in flux, known as a maser flare, may take 6-8 light days before its effects show up in the other shell, giving us the distance between the shells (Bowers et al. 1983). Shells typically measured around 10^{15} - 10^{16} cm. If we can measure the angular distance between the top and bottom maser shells, we can infer that this distance is equivalent to the distance between the front and back shell and through trigonometry determine the distance to the OH/IR star.

1.1.6 Planetary Nebulae

Planetary nebulae are the remnants of dead stars that are less massive than the ones that go supernova. They form over hundreds of thousands of years from the material that is pushed off of stars in their late stages. When a star stops fusing hydrogen in the core, the core contracts and heats up, thereby increasing pressure. Hydrogen outside the core (occupying much more volume than the core itself) will begin to fuse, supplying much more energy and heat. This heat expands the star, causing low surface gravity. From this stage up until the star death, mass loss processes take a major role in how planetary nebulae form.

There are many possible mechanisms which can be responsible for high amounts of mass loss.

Large pulsations may push material out to extreme distances. Fusion occurring potentially in multiple layers can cause large amounts of energy that escape through the layers of the star. This causes strong radiation pressure (stellar winds) and when combined with low surface gravity, can peel away the outer layers of a star by dragging material. Thermal pulsations could carry away the outer material on a much grander scale. The picture is quite complicated and the exact details are not known, but what has been pieced together is this mass eventually feeds into the forming planetary nebula.

Stars begin and end with nebulae. They are formed from them, and when they die, they create them. Through this process, stars and nebulae have become enriched with heavier materials that change the composition of the next generation of stars and overall galactic composition.

1.1.7 Knowledge Gaps

Despite all that we have been able to learn about the life cycle of stars, there remain innumerable gaps in our knowledge. The mass loss processes of stars, in particular, pose many as yet unanswered questions, such as:

1. How do spherical stars evolve to become asymmetric nebulae?
2. How do we model or predict mass loss rates in stars?
3. What do these processes look like at each layer of the star?
4. How can the structure of mass loss in asymptotic giant branch stars be observed?
5. Why are the mass loss processes more effective in some stars than others, affecting their evolutionary sequence?

This study hopes to contribute to the scientific conversation about these questions.

Most planetary nebulae are not perfectly spherical (see Fig. 1.3). Current models for mass loss in asymptotic giant branch stars assume spherical mass loss and are not capable of producing the variety of observed planetary nebulae. Evidence shows that mass loss does not occur at a steady rate and is not consistently uniform (Fong et al. 2002, Migenes et al. 1991, Bowers et al. 1983). In fact, uniform mass loss in stars is the exception, rather than the norm. As it currently stands, the scientific community lacks sufficient high-resolution observations to further constrain mass loss models.

As far as modeling the mass loss processes, it is necessary to determine what it looks like at each layer of the star. In that way, we can determine the effect that outer layers have on mass loss from inner layers. Perhaps the forces that create mass loss are more uniform than the various shapes of nebulae imply, but are simply unevenly effective, depending upon the layer that is being drawn away.

Mass loss processes are important in stars because they change the outcomes of the evolutionary path of stars. As an example, an intermediate star thought to be destined to become a neutron star could lose enough mass to end up as a white dwarf. Other intermediate stars through mass loss prevent their cores from exceeding the Chandrasekhar limit and they evolve on to fusing heavier elements.

One difficulty in studying the mass-loss processes is the presence of dust. When stars shed mass, it can form obscuring clouds or even shells of dust around the dying star that obscure all optical light, making it difficult to obtain a full picture of what is occurring at the stellar surface on a chemical and physical level. While limiting, this does not mean that there are no other options to effectively study these stars.

Planetary Nebulae

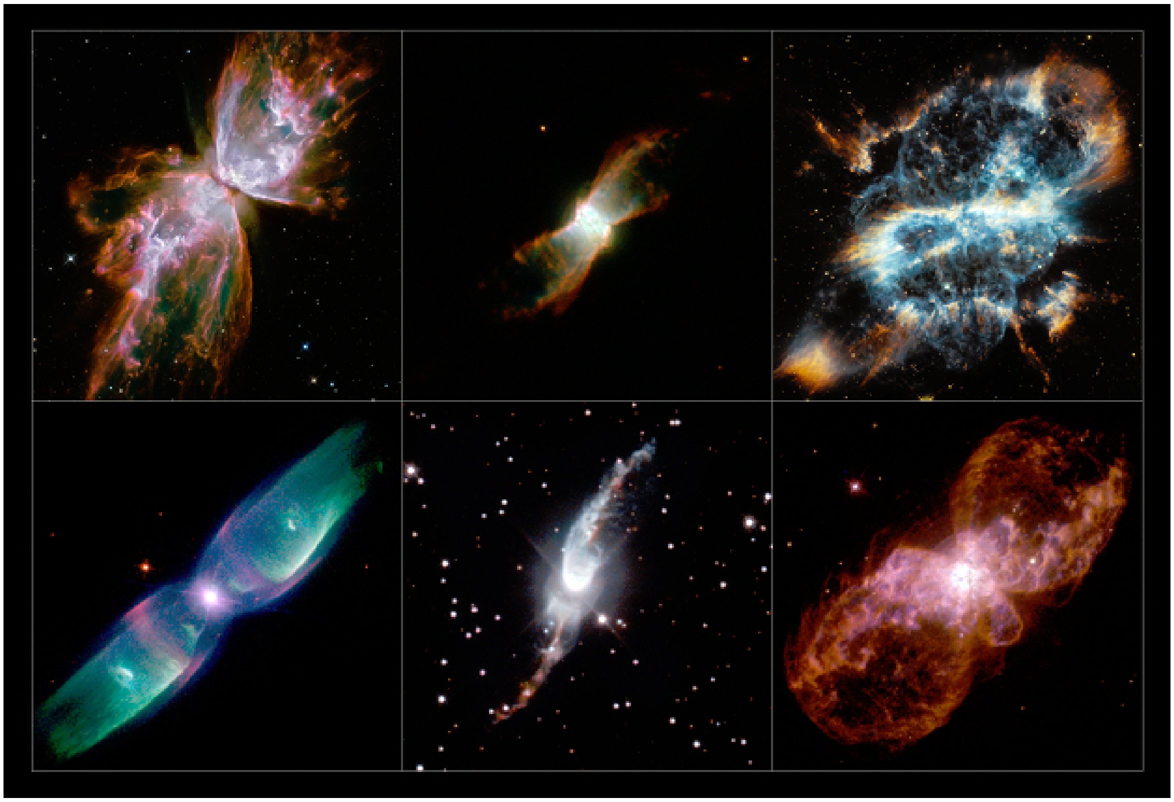

Figure 1.3 Planetary Nebulae displaying non-spherical evolution. Row 1 (from upper left): NGC 6302, NGC 6881, NGC 5189 Row 2 (from lower left) : M2-9, Hen 3-1475, Hubble 5
ESA/Hubble & NASA
NGC 6302: NASA, ESA and the Hubble SM4 ERO Team
NGC 6881: ESA/Hubble & NASA
NGC 5189: NASA, ESA and the Hubble Heritage Team (STScI/AURA)
M2-9: Bruce Balick (University of Washington), Vincent Icke (Leiden University, The Netherlands), Garrelt Mellema (Stockholm University), and NASA/ESA
Hen 3-1475: ESA/Hubble & NASA
Hubble 5: Bruce Balick (University of Washington), Vincent Icke (Leiden University, The Netherlands), Garrelt Mellema (Stockholm University), and NASA/ESA
http://sci.esa.int/hubble/52821-a-selection-of-hubbles-planetary-nebulae/ .

1.2 Studying the Mass Loss Processes

There is a lot that can be done to study the mass loss processes at non-optical wavelengths to help fill in some of the gaps in our understanding of how the mass loss processes affect stars and future star formation. A dusty shell will shift the star's spectral energy distribution to the infrared and can reveal how rich in dust these environments are. Even the shapes of the dust shells have proved helpful in determining the uniformity of the mass loss. Certain molecules in this shell, like CO for example, emit in the radio at 2.6 and 1.3 mm wavelength transitions and abundances of this molecule feed into mass loss estimates. The presence of masers allows us to study the shapes and chemistry of maser shells through radio telescopes at incredible distances. Although optical light is blocked by the particles of a dying star's dust shell, recent techniques have been able to measure dust clouds blocking signals in order to obtain valuable information. Below are several means of study and some of their benefits and shortcomings.

1.2.1 Masers

Masers are Microwave Amplification by Stimulated Emission of Radiation. Masers naturally occur in astrophysical environments from molecules that have a metastable transition. These transitions have energies that correspond to radio or microwave photons. Warm (450 - 1500 K), dense ($> 10^7$ cm^{-3}) regions of molecules that have these metastable transitions are able to redirect large portions of incoming energy to the metastable energy transition of the molecule. This causes their energy signal to be amplified and the movement of the medium releases this amplified signal in the direction or anti-direction of the medium's velocity.

In order for the gaseous region to exhibit masers, molecules must have an energy source or pumping mechanism to be excited to this metastable state. This energy source could include radiation from a nearby star or high kinetic energy allowing for the molecules to be collisionally excited. Because the density is high when a molecule does emit a photon and drop to the ground state, the photon is likely to be absorbed quickly by surrounding molecules. Due to this previously mentioned condition and this state being stable for long periods of time, a continual supply of energy will cause more molecules to be in the higher state than the ground state, known as a population inversion.

Stimulated emission occurs when nearby photons of similar energy to a transition resonate with a given molecule to invoke its transition. This multiplies or amplifies the number of photons at the particular transition energy. If the medium was not moving we would have a region of random photons at a particular energy being constantly absorbed and emitted, but a moving medium provides an energy shift for the emitted photon. The medium's forward or backward direction gives the photon a means to escape. These preferential escape directions beam the energy, making a strong, intense signal. This process is known as masing.

OH/IR stars exhibit masers from molecular types of H_2O, OH, and SiO that form gaseous shells around the star and have a metastable state similar to lasers. The metastable state for each of these molecules is a rotational state. For OH molecules the pumping mechanism includes radiative processes that occur around temperatures of 450 K and densities of 10^7 cm^{-3}. For H_2O the pumping mechanism includes collisional processes that occur around temperatures of 750 K and densities of 10^8 cm^{-3}. For SiO, the pumping mechanism is a mixture of radiative and collisional processes that occur around temperatures of 1500 K and densities of 5 x 10^{10} cm^{-3}.

When the shells of OH/IR stars reach the right density and temperature, they will mase. We can observe this in the radio part of the electromagnetic spectrum. Masers create strong signals that can be observed from incredible distances using radio telescopes and are typically very compact sources. Interferometry is a method to study masers at high spectral and spatial resolution and is the method used in this dissertation. This method allows for mapping the maser shell and can probe the uniformity of these shells at different scale sizes.

1.2.2 Infrared

OH/IR stars have dusty environments which cause the star's underlying spectral energy distribution to be shifted from the optical to the infrared. The infrared fluxes reveal details about how much dust is present in the regions and has been the primary tool to discover OH/IR stars by identifying dusty sources and checking for radio OH masers (te Lintel Hekkert et al. 1991). As OH/IR stars become more evolved, more dust forms around the star (Habing et al. 1989). The dust envelope is also emitting radiation and can be studied to probe the circumstellar structure (Ruiz-Velasco et al. 2011). Ruiz-Velasco characterized the emitting portions of three southern hemisphere OH/IR stars, measuring the fluxes and sizes of their emitting dust shells.

1.2.3 CO Emission

Regions around stars that have pushed carbon and oxygen into their circumstellar envelopes can be studied by mapping out the CO emission. CO is known as a trace element for its property of being proportional to the amount of molecular hydrogen. CO is a tightly bound molecule and has radio transitions at 2.6 and 1.3 mm wavelengths (Sanchez Contreras et al. 1998), which makes it useful to probe the extent of the dusty regions around asymptotic giant branch stars. This has yielded envelope size measurements as well as mass loss estimates for asymptotic giant branch stars (Neri et al. 1998) but is less reliable for highly evolved stars or stars with a high mass loss because the emission becomes too diffuse to detect or because a key assumption fails to hold - the number density of CO scales well with other elements. Because of these shortcomings, we opted not to use this method for the purposes of this project to constrain modeling the mass loss processes.

1.2.4 Optical

OH/IR stars have characteristic shells of dust around them, making a direct optical observation difficult (Mauron & Huggins 2006, Mauron et al. 2006). This is why, when using optical telescopes, we study not the OH/IR star cloud itself, but use the optical telescopes to measure what the dust cloud blocks. When the cloud is observed, we compare any measurements of light to the average galactic photon background, a kind of "background light pollution" found throughout the galaxy. Once compared, the difference can be used to determine how much of this background is being blocked by the dust cloud, and thus the density, shape, and size of the dust shells.

Unfortunately, the amount of information that can be extracted from this data is limited and does not lend itself to studying more than the size, density, and shape of the dust shell. Another difficulty is a relative scarcity of instruments able to detect the average galactic photon background, as well as the large amount of time needed to observe this background, making observation time difficult to obtain. If field stars are in the field of view, they can also interfere with observation and be difficult to subtract out of obtained data. We attempted to use this method with the Brigham Young University West Mountains 0.9-meter telescope but could not get low enough noise measurements to measure dust shells blocking the galactic background.

1.2.5 Interferometry

Interferometry is the process of combining light signals from multiple locations. This can yield high-resolution observations by extending the sampling locations over long distances. The projected distance between any of these locations is called a baseline as viewed from a source. Larger baseline relates directly to the smallest angular scales that can be probed, thus providing high resolution.

$$\theta_{min} = 1.22 * \lambda / D \tag{1.1}$$

Where θ_{min} is the minimum resolvable angle, λ is the wavelength, and D is the baseline distance all in SI units. Even though achieving this high resolution is equivalent to the resolution of building an antenna with a diameter the size of the baseline, the light gathering power is not the same. The light gathering power is still dependant on the area of the combined antennas. So on this note, having many antennas making a contribution to measuring the strength of a light signal or flux energy density of a source is useful. A single baseline only gives high resolution in one direction, but this is easily remedied if you have many baselines present and allow the earth's rotation to naturally change the baseline orientations to sample the source. By sampling a target at many different baselines in many orientations provides a way to construct an estimate of what an aperture would see that would have a diameter as big as the largest baselines without having to build such a thing.

1.3 Mass Loss

Asymptotic giant branch stars may lose 35 - 85% of their mass in this stage (Decin et al. 2006), feeding complex circumstellar shell structures and making this stage one of the most interesting and detrimental in a star's evolution. Stellar winds are thought to be the primary cause of the sustained mass loss but their geometries are not well constrained. Large mass loss can occur through thermo-pulsations with periods of 10,000 - 100,000 year (Decin et al. 2006). Mass loss is postulated to increase with time (Marshall et al. 2004) as the luminosity increases. Asymptotic giant branch stars end in a superwind phase and experience mass loss increases by factors of 100 - 1000 (Schöier et al. 2005) over 100 year periods. One explanation for these high variations may be feedback between the wind acceleration rates and the dust formation (Simis et al. 2001) These mass loss episodes are far from being understood but are linked with the formation of planetary nebulae.

The mass loss has been observed to be symmetric in some cases and in others asymmetric but the exact details are not known well enough to model a star's evolution into a planetary nebula (Fong et al. 2002, Migenes et al. 1991, Bowers et al. 1983). Bowers claims that models for single stars or binaries cannot predict the distribution of features we observe in the circumstellar shells and has even seen a rare disk-like geometry. Zijlstra et al. (2001) has suggested that a faster equatorial wind from the post-asymptotic giant branch stage may be responsible for such developments. Vlemmings et al. (2005) has detected large-scale magnetic fields that permeate the circumstellar regions and has investigated them being a significant driver of evolution.

1.3.1 Ways of Determining Mass Loss

Multiple methods have been proposed for determining mass loss rates for OH/IR stars. Netzer & Knapp (1987) proposed that we can predict mass-loss rates by determining the OH mass loss. This involves assuming a n_H/n_{OH} ratio, spherical mass loss, measuring the expansion velocity and mapping the OH maser shell to get its location. Another approach involves measuring the location and velocity of the OH maser shell, the velocity of the central star, the thermal velocities of the shell and inferring maser saturation (Bowers et al. 1983). Another method relates the OH luminosity and shell velocity to the mass loss (Baud & Habing 1983). Finally, Wachter et al. (2002) proposed that mass loss can be derived from stellar temperature, luminosity, and mass for carbon-rich stars.

Although these models are useable, these models ignore effects of non-uniform mass loss. In addition, the model proposed by Wachter et al. (2002) has not been adapted to the chemistry of OH/IR stars. This is due to the fact that detailed and systematic measurements of the properties of these shells do not exist. With models that are not well constrained, it is no wonder that predictions from different mass-loss models for evolved stars can sometimes differ by a factor of 100 (Habing et al. 1989).

1.3.2 The Mass Loss Processes in the Scientific Community

Once we are able to observe and understand the mass loss processes more fully, we will be able to constrain models for the mass loss processes. A more thorough understanding of these processes will allow us to understand how stars die, and more about what their late stages look like and how to predict what each star will do in its late stages. It will allow us to estimate and map the shapes that a star may assume at the end of its life, and the shape of any resulting nebula. We will also be able to understand how material from stars drifts or is pushed into the interstellar medium which eventually will be incorporated into future stars and planets.

Low-resolution studies have revealed non-uniformity in OH/IR stars, but fail to provide detailed structural measurements. For example, Herman et al. (1985) observed 10 galactic-plane OH/IR stars at VLA 1.0" resolution and noticed the typical 1612 MHz OH deviation from spherical symmetry were less than 20%. Although this symmetry was measured, the radial distances to the shells and uniformity of the shells were not measured. Without specific measurements like those aforementioned, we will not be able to provide structural details of shell uniformities, which would discriminate mass loss models. We deduced a need to probe deeper (higher resolution and closer targets) and probe stars hinting slightly more advanced stages to extract the details for improving mass loss models.

1.4 Hypothesis

1.4.1 Motivation

Our intent is to map out the circumstellar shell structure for multiple shells surrounding OH/IR stars so that we can understand their morphology and so that better mass loss models of these types of stars can be obtained. We targeted six highly luminous OH/IR stars and planned to map out the maser emission to probe for various environmental conditions. The locations of the masers trace out denser portions of the molecular circumstellar shells and are used in some models to estimate mass loss rates. Through probing this structure we will measure the amount of uniformity that occurs through different layers in the star. Next, we can estimate the mass loss rates using Netzer's model. Finally, we can extend the model provided by Netzer & Knapp (1987) with our uniformity measurements to better estimate the mass loss and model how it affects different portions of the circumstellar envelope.

1.4.2 Impact

With this study, we can create better models for asymptotic giant branch stellar evolution. We will measure the shell uniformity and thickness at specific spots inside the OH maser shells and model how these parameters relate to the mass loss rates. Having this data will help future models account for evolving shell uniformity, which directly correlates to accurately modeling planetary nebulae formation.

Chapter 2

Experiment Design

2.1 Original Experimental Design

At the original onset of the project, we had recently been given access to infrared interferometric Very Large Telescope data of three OH/IR stars in the southern hemisphere. These data produced measurements of the sizes of the circumstellar dust shell that was emitting in the infrared. We were unable to receive time on the Long Baseline Array, a radio interferometer in the southern hemisphere, to further study these objects, so we opened our search up to targets in the northern hemisphere that would be great candidates for probing structure.

2.2 Actual Experimental Design

We searched through 738 OH/IR stars classified by te Lintel Hekkert et al. (1991). Te Lintel Hekkert et al. had performed a follow-up survey on Infrared All-Sky Survey (IRAS) sources that registered a high amount of dust indicative of OH/IR stars. They used Germany's Effelsberg and Netherland's Dwingeloo telescope in the northern hemisphere and Australia's Parkes in the southern hemisphere. They surveyed the 1612 MHz OH maser line and found 139 of the IRAS source locations corresponded with a spectral profile of an OH/IR star. I looked through 139 of these sources archival data to note whether each source had been observed by the Very Large Array, Very Large Baseline Array, Green Bank Telescope, Herschel Space Telescope, and Hubble Space Telescope and if their positions were part of the 2Mass survey. I also noted the wavelength bands that these sources were studied at with high resolution and any published distances to these OH/IR stars. Most notably not a single target had 1720 MHz observations and only one had 22 GHz observations for H_2O. There was a project that surveyed 17 of the targets for a very short period of time, useful for sampling the spectra and one source IRAS 01304+6211 that had been studied by 4 projects at greater length. I reduced one of the data sets for IRAS 01304+6211, but due to the setup of the experiment not using a phase reference calibrator, the masers mapped lacked sufficient dynamic range to obtain specific details to measure structure, uniformity, and estimate mass loss.

Of the 139 OH/IR stars, we chose to focus on these six: IRAS 21554+6204, IRAS 22177+5936, IRAS 01304+6211, IRAS 03206+6521, IRAS 03293+6010, and IRAS 05073+5248 (see Tab. 2.1). I looked for targets that indicated they were highly evolved, viewable by the Very Large Baseline Array, and were close enough so that the resolution of the Very Large Baseline could resolve structure in the OH shell at 1.6 GHz and the H_2O shell at 22 GHz. Although few had distance determinations, a handful could be resolved by the VLBA. We did choose one target without a distance determination, but that had high potential to yield resolved structure when comparing its attributes to other sources. All targets chosen have the high potential for strong dust formation indicated by comparing their IRAS fluxes (see Tab. 2.2). I compared the 25-micron flux of these sources to the 12-micron flux by dividing them to come up with a ratio I defined as the dust factor and used this to pick the dustiest sources.

Table 2.1 Source Posistions and Distances

IRAS Name	RA	DEC	Galatic Long.	Galatic Lat.	Dist. (kpc)	Dist. Source
21554+6204	21:56:58.3	+62:18:42.0	104.130	5.991	-	-
22177+5936	22:19:27.5	+59:51:20.0	104.908	2.413	2	Palagi 1993
01304+6211	01:33:50.7	+62:26:46	127.814	-0.023	5.6	Palagi 1993
03206+6521	03:25:08.7	+65:32:03.0	137.971	7.255	2.4	Bowers 1983
03293+6010	03:33:30.7	+60:20:09.0	141.725	3.519	3.7	Bowers 1983
05073+5248	05:11:19.5	+52:52:33	156.438	7.835	0.82	Palagi 1993

Table 2.2 Source and Fluxes

IRAS Name	Flux 25 μm (Jy)	Flux 12 μm (Jy)	25 μm / 12 μm flux	OH physical resolution(cm)	H_2O physical resolution(cm)
21554+6204	150	67	2.24	-	-
22177+5936	250	130	1.91	1.4E+14	1.0E+13
01304+6211	460	92	1.41	1.7E+14	1.2E+13
03206+6521	130	92	1.41	1.7E+14	1.2E+13
03293+6010	70	38	1.86	2.6E+14	1.9E+13
05073+5248	270	220	1.20	5.8E+13	4.2E+12

2.3 Data Collection

We observed six OH/IR stars using the very long baseline array (VLBA). The VLBA (see Fig. 2.1) provided long interferometric baselines to probe useful radii of the shell structure. Due to the rarity of OH/IR stars, even the closest ones need high-resolution data to measure circumstellar radii. The task could only be done by a handful of instruments (European Very Long Baseline Interferometry Network and the Long Baseline Array being two others). The VLBA was chosen for its 10 antennas of similar design and its long baselines, providing high resolution. Each antenna is 25 m in diameter. The VLBA is located in the Northern hemisphere, mainly spreading across the mainland United States with sites in Hawaii and St. Croix, US Virgin Islands. The longest baseline is from Mauna Kea, Hawaii to St. Croix for a stretch of 8611 km. It is at an average declination of 33 degrees north. The angular resolution for the VLBA at 1.6 GHz is 4.70 milli-arcseconds and at 22 GHz is 0.345 milli-arcseconds from equation (1.1).

Very Large Baseline Array

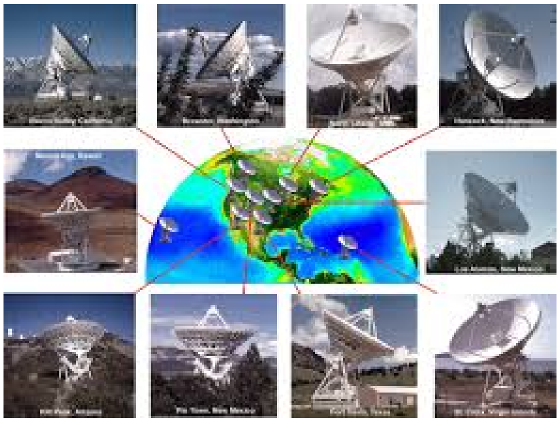

Figure 2.1 The Very Large Baseline Array antennas and their locations across the United States and territories. From http://images.nrao.edu/images/vlba_montage_lo.jpg .

We observed our targets using a nearby phase reference. Phase reference experiments involve observing a nearby target with steady flux measurements which have a higher flux density at the wavelength of interest. This phase referencing target (or calibrator) is observed multiple times interspersed in between the target of interest. After the data sets are correlated, the phase of the phase calibrator is corrected for several factors such as rate and delay. It is easier to model corrections on the phase referencing calibrator and apply these same modeled corrections to the source of interest. These corrections are needed because the atmosphere for which light has to travel through for each antenna varies through time and is location dependent (fixing the rate). Different frequencies are also affected differently while traveling through the atmosphere (fixing the delay). Atmosphere changes at 1.6 GHz are normally stable on the order of 10-20 minutes. We set up our observing schedule to observe the phase calibration for 2 minutes out of every 7 minutes to track changes in time throughout our experiment. The atmosphere at 22 GHz can change in a matter of minutes, so we observed our phase calibrator for 30 seconds out of every 1.5 minutes. Tracking detailed phase measurements in this way throughout the experiment increases the dynamic range of mapping, which will allow us to probe smaller scales more accurately when studying the structure. For probing positional structure, sharing the observing time with a good phase reference calibrator provides greater dynamic range when mapping emission than observing 100% of the time on the source.

We collected our first set of data Aug 14, 2015. We observed two targets. We subsequently collected more data Feb 21, 2016, on 4 more targets. There were two groups of two targets each that were able to share phase reference calibrators, which allowed us to increase actual time on our targets.

We observed the 22 GHz maser transition of H_2O and four of the maser transitions of OH (1.612, 1.665, 1.667, 1.720 GHz) in spectral line mode. For H_2O and OH we used 4 MHz and 1 MHz bandwidth respectively. For OH we observed in Dual polarization mode with 1024 spectral channels. For H_2O we observed in LCP mode with 1024 spectral channels. As our amplitude flux calibrator, we used 3C48, a VLBA standard. And for phase reference calibrators we used J0339+6008, J2148+6107, J0458+5508, and J0109+6133.

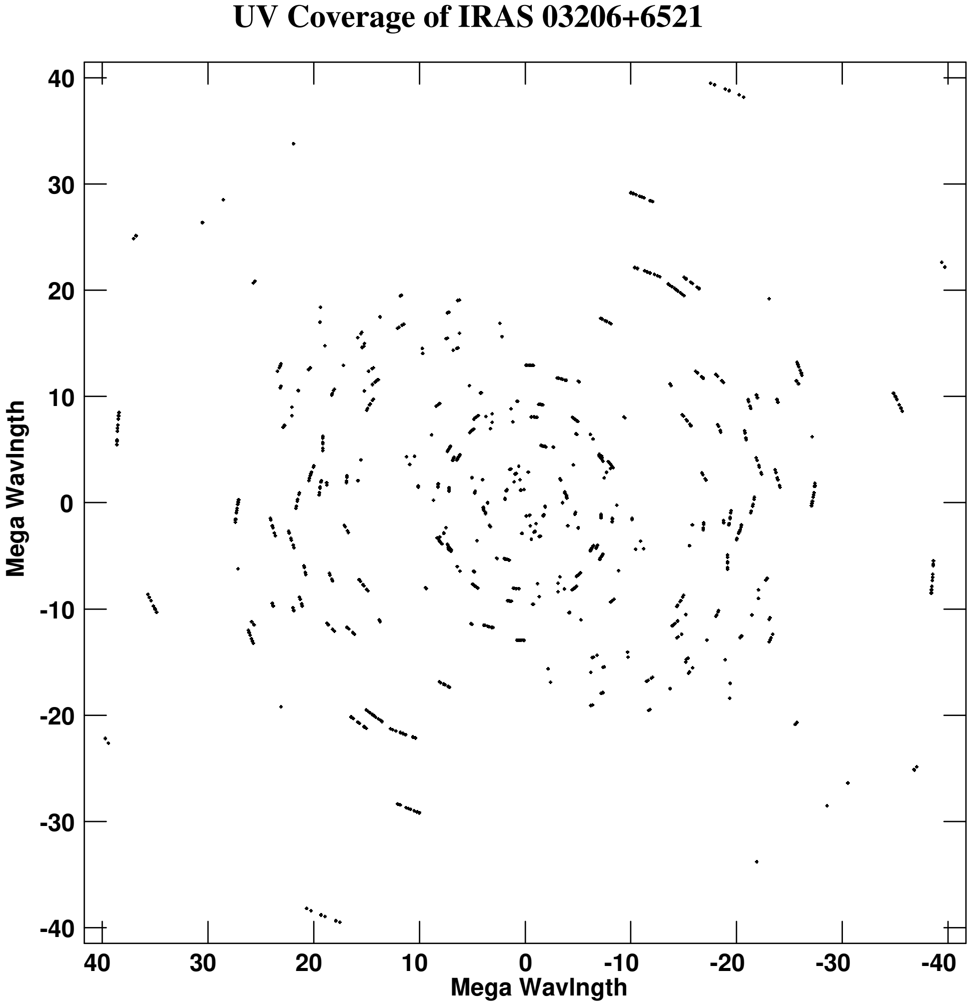

Figure 2.2 UV coverage map of IRAS 03206+6521. This represents the plane in the sky toward the source that was sampled. Each dot represents a baseline distance and orientation from the center of the array where the UV plane was sampled.

The data were correlated with the Socorro-DiFX correlator. The setup was 2 second time averaging for H_2O and 6 seconds for OH. Frequency widths for OH were 0.97 kHz/channel. Frequency widths for H_2O were 3.9 kHz/channel

We estimated our image sensitivity to be a very impressive 0.69 Jy and 0.23 Jy for H_2O and OH. This is sensitive enough to detect even some very weak features from the masers.

Chapter 3

Data Analysis

We loaded our data into the Astronomical Image Processing System (AIPS) program which has procedures available to handle calibration steps for radio interferometric data and tools to view the data in useful ways. The steps taken to reduce are as follows:

1. FITLD: Load data into AIPS
2. CLCOR: Correct for ionosphere path lengths and opacity.
3. POSSM, EDTR, LISTR, VPLOT: Inspect the amplitude calibrator in several ways and flag any bad antennas, times, or baselines.
4. ANTAB, APCAL Correct the amplitudes for the amplitude calibrator and apply the corrections to all sources.
5. POSSM, EDTR, LISTR, VPLOT: Inspect the phase calibrators in several ways and flag any bad antennas, times, or baselines.
6. FRING, CLCAL: Correct rate and delay errors for the phase calibrators and apply the corrections to itself and its associated target source. Solutions to correct the phase are needed frequently and correct data over short time intervals.

7. POSSM, EDTR, LISTR, VPLOT: Inspect the source in several ways and flag any bad antennas, times, or baselines.

8. FRING CLCAL: Correct the rate for a strong channel from the target and apply the correction to all channels.

9. BPASS: Calculate a bandpass on a continuum source and apply the correction to all sources. The side channels need to be thrown out because the bandpass correction performs poorly on the end channels.

10. CVEL Correct the frequency data for Doppler-shifting for all sources due to the antennas traveling at different speeds with respect to the source because of earth's rotation.

11. SPLAT, IMAGR, CALIB, CLCAL, CCMRG: Now we can map the phase calibrators and run through self-calibration. This involves averaging the phase calibrator data in frequency and imaging it to give this as the first model for the data to fit. In this process, the emission peaks for the model are specified. Phase adjustments are calculated to bring the data into conformity with the model. If this improves the imaging one can further build on this image as the new model, otherwise one builds the model differently until successful or until no more improvements can be made. The data that does not fit the model is clipped or cut to improve convergence to a good image. The phase corrections to achieve this are then applied to itself (the non-averaged data) and the target sources.

12. IMAGR, CALIB, CLCAL, CCMRG: Another round of self-calibrating takes place but this time the target source is self-calibrated.

13. SPLIT, IMAGR: Each channel is mapped. This produced nearly 1024 maps in our experiment. Each map represents a particular picture of the star and its regions at a specific frequency which we can convert to represent the Doppler-shifted velocity. This

we interpreted and used as a tool to measure what speed material is moving with respect to the reference frame velocity (referring to the OH/IR star's frame).

3.1 Determining the Uniformity

At this point, we have spectral line profiles and intensity maps of the regions observed for the sources with detections. The program used to reduce the data did not have sufficient tools to complete my analysis so I wrote a python program to extract the intensity of every image pixel to perform a uniformity analysis.

I first identified all the images with emission and averaged some of them which were close in frequency to get a higher signal to noise ratio. After finding that the center of intensity was not the same as the star coordinates and did not always match the opposite shell, I entered in a step to calculate the center of intensity. I trimmed out the central pixels because one bad high pixel could easily bias the average. In some cases I restricted the angular start and stop points to "zoom" in on the actual emission. I looked into throwing out high points, but they did not affect the results. I did throw out any negative flux values because they seemed to be bad points that were not removed at the data reduction stage but should have been.

From this point, I cut the data into thin concentric rings (see Fig. 3.1) (I found 2 pixels thick worked best). I summed up the intensity of each ring and divided by the total number of pixels in the ring and plotted this average intensity per pixel value versus radius (see Fig. 3.2). That is equivalent to projecting onto the angular axis. Then I identified the peaks in this plot (representing maser shells) and fitted Gaussian profiles to them and subtracted the excess noise and continuum emission (see Fig. 3.3). This gave estimates of the overall average shell thickness and distance from the center of intensity. I repeated the same method of fitting the local shell thickness and distances on smaller angular scales (typically 2 degrees) across the entire angular spread that was used to determine the overall average (e.g. over 360 degrees).

For each of the local measurements, I compared them to the overall average and classified them as uniform or non-uniform. A local measurement would be classified as uniform if the central peak of the locally fitted Gaussian fell within 2.5 times the full width at half maximum (FWHM) of the overall Gaussian fit, the local Gaussian fit was positive, and the local Gaussian fit FWHM was not larger than 3 times the overall average FWHM. Uniform portions then contribute their angular size to the overall percentage of uniformity of the overall angle. As an example, if two 5 degree segments of 180 degrees were classified as uniform, then the uniformity of this feature is $5*2/180$ or 5.6%.

To graphically show the uniformity fits of each image, I plotted the image and overlaid helpful drawings to visually interpret the analysis (see Fig. 3.4). Three yellow circles are drawn, the middle representing the overall Gaussian peak, and the inner and outer representing the FWHM. The tick marks on the extreme outer edge of the image represent the angular resolution used to slice the image into pie slices. On each angular slice, a Gaussian analysis is performed and marked green for a positive match (meaning the slice's Gaussian fit falls within the overall Gaussian fit) or red for no match. Within the angular area on the green ticks, there is a green line representing the location and FWHM of the fit. The uniformity is then determined by adding up all the positive matches and multiplying by the angular space they occupy and dividing by 360 degrees.

After the uniformity analysis of each map, I defined several parameters to describe the circumstellar regions including the thicknesses, uniformities, Doppler-shifted velocities, and off-axis radial distances to shells (derived from the image's x and y axis). Herman et al. (1985) measured the distance to the OH maser shell in IRAS 03206+6521 as $3.43{*}10^{16}$ cm. With this shell distance measurement, we iteratively scaled our map velocities to radial distances (z-axis) to each map. Faster velocity maps were scaled slightly radially inward from the estimated shell distance measurement while lower velocity features were scaled to be slightly further. These radial distances were fed into one of Netzer's mass loss equations (3.1) (equation 12 in his paper) adapted to stars like IRAS 03206+6521 to obtain the mass loss rate,

$$M_{\odot}/yr = (r/3.9 * v^{0.4})^{1.43} * 10^{-5} \tag{3.1}$$

$M_{\odot}$/yr is the mass loss rate in solar masses/year, r is the radial distance (in x10^{16} cm) from the star, and v is the Doppler-shifted velocity (in km/s). The radiation parameter was chosen to be 3.9 signifying a high radiation field. This parameter comes from models needing to account for different radiation fields the location and velocity of the OH maser shells (Netzer & Knapp 1987). This produced mass loss estimates at six different maser shell locations. We compared this with the uniformities and thicknesses to study their relationships.

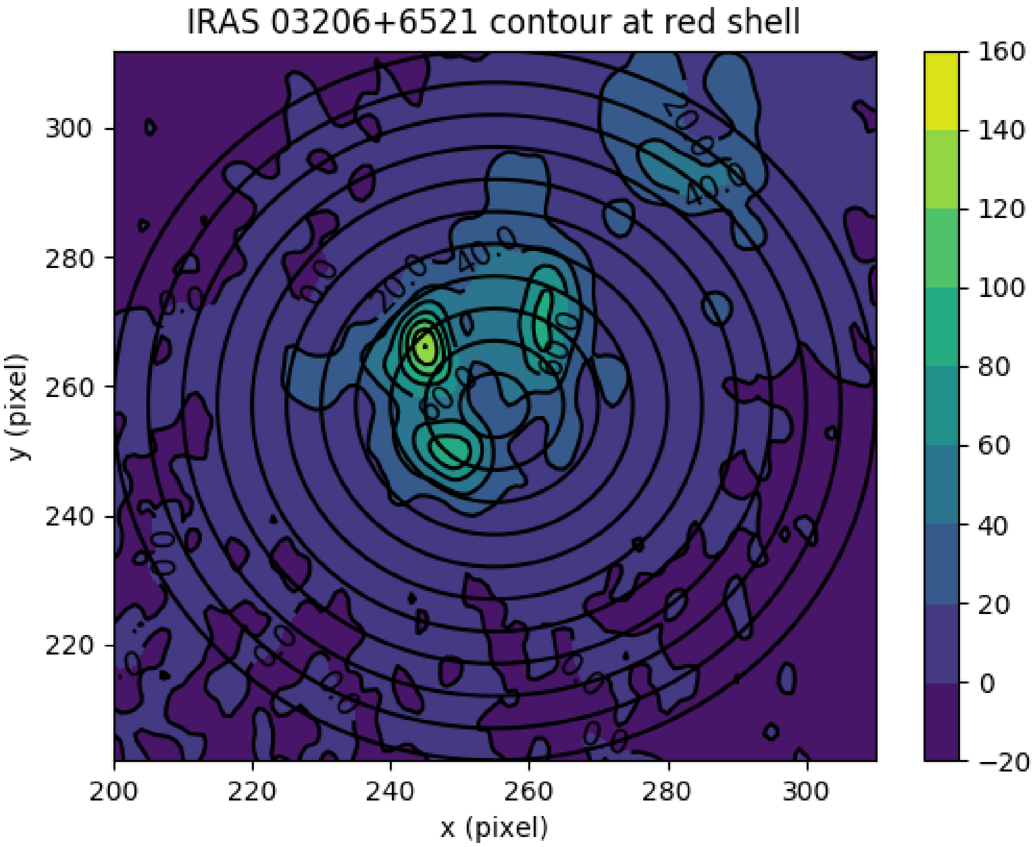

Figure 3.1 Color contour intensity map of IRAS 03206+6521 centered on the IRAS source at 1612MHz of the red shell region. Velocity 9.8 km/s (star's reference frame). Pixel scale: 1 pixel is 1.2 arcsec. Intensities are in millijansky. The black lines represent concentric ring slices; the actual slices were much finer and if shown would conceal too much of the image.

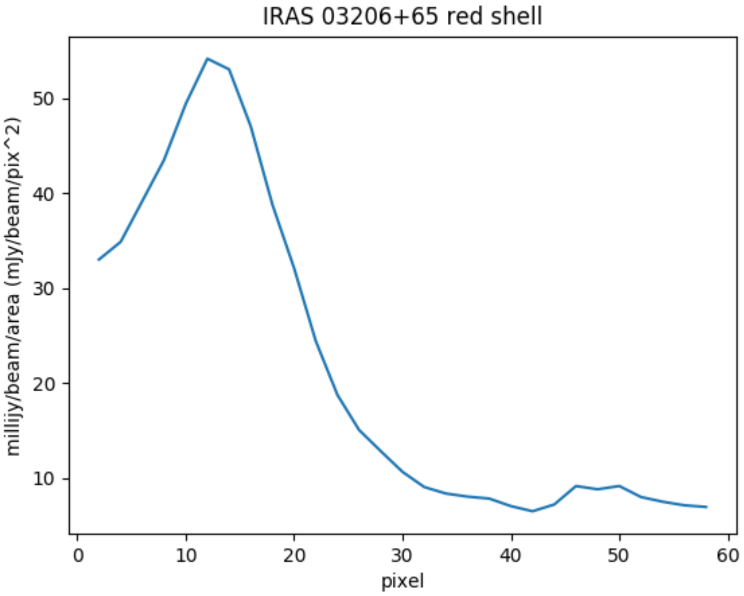

Figure 3.2 Radial plot of the 1612 MHz emission of IRAS 03206+6521 of the red shell region. Intensity in concentric rings is totaled then divided by the total area within the ring.

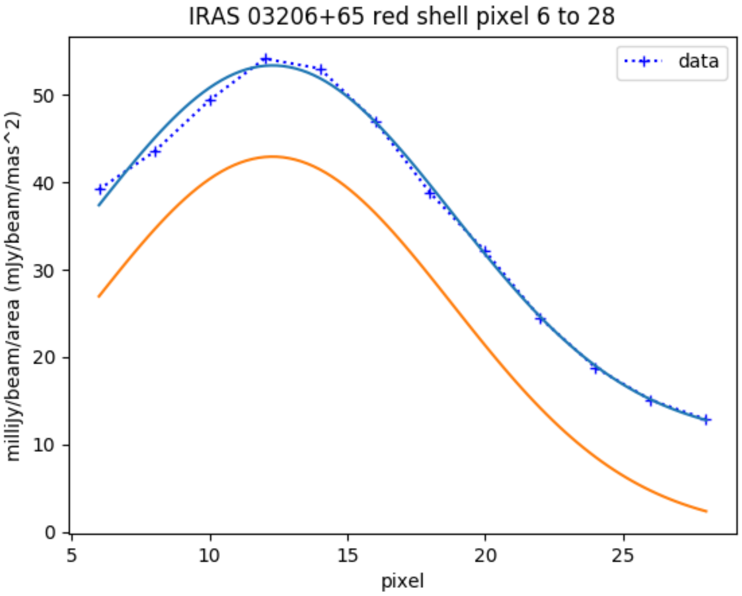

Figure 3.3 Gaussian fit to a particular radial range of the radial plot IRAS 03206+6521 of the red shell region. Blue plus signs represent the data points. Dotted blue lines are a linear interpolation between data points. The solid blue line is the fit. The solid orange line is the fit with which the continuum or offset above zero was subtracted.

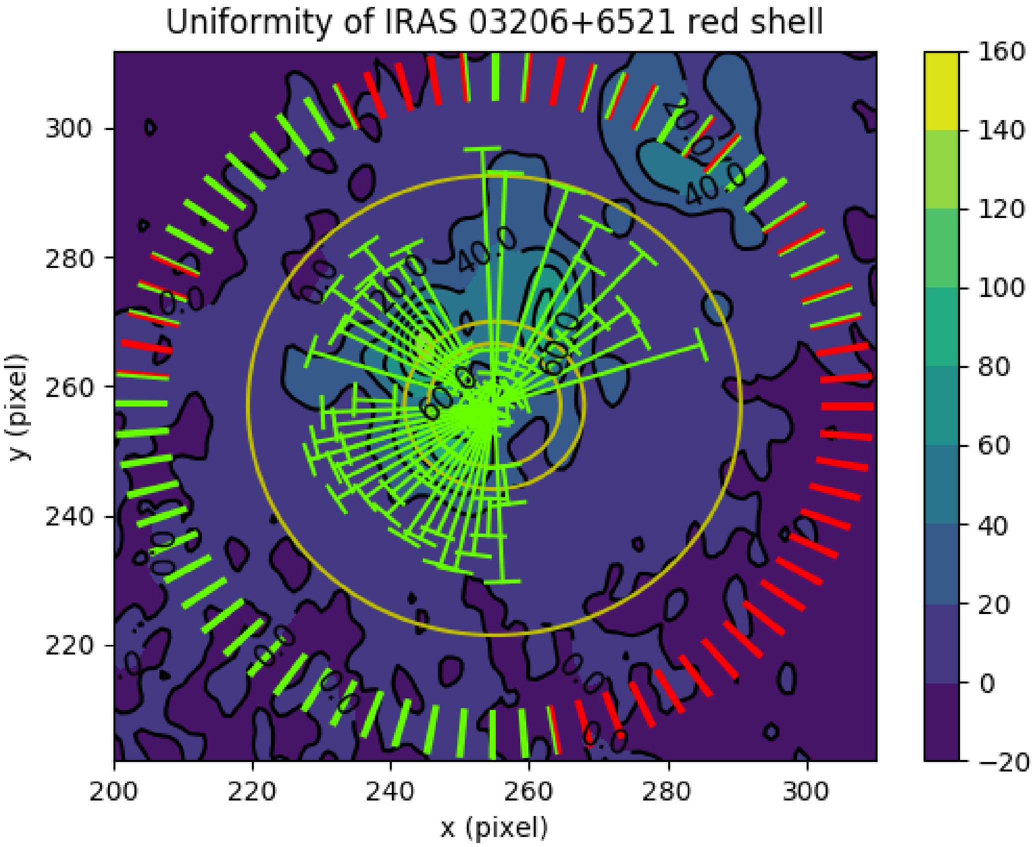

Figure 3.4 Gaussian fits to IRAS 03206+6521 overlaid on the intensity map to show the uniformity of the red shell region at velocity 9.8 km/s (star's reference frame). An overall Gaussian fit peak is represented by the central yellow circle. The edges of the overall full-width half maximum (FWHM) fit are represented by the inner and outer yellow circles. The tick marks on the extreme outer edge of the image represent the angular resolution used to slice the image into pie slices. On each angular slice, a Gaussian analysis is performed and marked green for a positive match (meaning the slice's Gaussian fit falls within the overall Gaussian fit) or red for no match. Within the angular area on the green ticks, there is a green line representing the location and FWHM of the fit. The uniformity is then the total number of uniformity slices times their angular resolution or the percentage they occupy on the whole image. This maser shell showed a uniformity of 60.6%. The actual slices in the analysis were much finer than shown (2 degrees versus 5 degrees) to better visually demonstrate the technique.

Chapter 4

Uniformity Analysis Program

I developed the program and technique used to run the uniformity analysis on the images in this dissertation. As such, I am making the code available because of the many applications it can have to astronomy and other fields. In this section I explain what the code does in detail, how to get the code, and how to run the code. Hopefully it is utilized to help solve different types of problems.

The program takes in a list of x, y, z representing the x, y image pixel coordinates and intensity (z) value for that pixel. The user specifies the central pixel with which to perform the uniformity analysis and the square width of the subimage to operate on. The user also specifies the pixel width with which to slice the image into circular rings. The program then reads the data and outputs a contour image with the radial cuts drawn (users can control the contour line values). There are options to ignore a certain percentage of the center, choose to analyze a specific continuous angular portion (like 47 degrees to 59 degrees), throw out high pixel values (user sets the threshold), throw out negative pixels, draw radial cut lines, and name the contour plot. There is an option to find the center of intensity using a user-defined percentage around a user-specified center pixel.

Now the analysis will visit every pixel in the sub-image and determine what ring cut it belongs to. It will add up the pixel's intensity and pixel area then divide by the total number of pixel area in each circular cut. A plot is generated to show the average intensity per circular ring cut (radial plot).

The user looks at the radial plot and determines where (the start and end pixels) to determine a Gaussian fit. The radial profile is then fit to a Gaussian using the scipy library and subtracts off the intensity offset (background continuum signal). This gives us the Gaussian full width half maximum and Gaussian peak location This is called the overall Gaussian fit. Now the code re-performs all the stages to reach a Gaussian fit on smaller angular segments (user specified) and this fit is compared to the overall fit. If the fit from the smaller angular slice meets the following three criterion its angular size contributes to the uniformity, otherwise, it does not. The criterion includes: the smaller angular slice peak location must fall within 2.5 FWHM of the overall fit peak location; The smaller angular slice FWHM must fall within 2.5 FWHM of the overall fit; The smaller angular slice fit must be positive.

The program outputs a graphical display of the uniformity and outputs a text file with the calculated values from the analysis.

4.1 Installing the Program

The uniformity analysis program runs on python (version 2.7 or 3.6) and requires pip (a python dependency installer). Both python and pip come standard with new versions of anaconda which can be obtained from https://www.anaconda.com/download/. Then python and pip should be added as system path variables in Windows.

The source code for running a uniformity analysis, which I use in this dissertation, can be downloaded from GitHub (https://github.com/dfelli/uniformity_analysis) which comes with a working example. To get the code running, download and extract the repository.

To install the python dependencies, navigate to the directory where you put the source code. Run:

```
pip install -r requirements.txt
```

4.2 Running Through an Example

To run the example:

```
python uniformity_analysis.py input_parameters.json
```

This should produce four image files in this directory to verify the code is running without error on the computer.

4.3 Adapting to Code Inputs for Different Data

Now one should open the input_parameters.json file with a text editor and adapt the code to individualized data. Here are the key parameters to set/update the data (JSON format):

```
"data_file" : "pixel_data_example",
"bin_size" : 5,
"pix_widthX" : 111,
"pix_widthY" : 111,
"centerX" : 255,
"centerY" : 257,
```

The data_file parameter is the name of the file containing the image's x y pixel coordinates with a z coordinate representing the intensity (square images only). The file must be formatted with the first line being (tab separated).

```
x	y	intensity
```

The following lines are actual x y intensity data as integer or floating point numbers. Order matters for the sequence of numbers. First, start with the lowest x y pixel numbers and increase the x pixel through its entire range. After this one should move on to the next y pixel. For example, the following is a crude 3 by 3-pixel image (tab separated).

1	1	2.368
2	1	-2.063
3	1	-4.584
1	2	-7.552
2	2	3.963
3	2	4.884
1	3	12.368
2	3	1.063
3	3	0.564

The bin_size parameter is the pixel separation with which to slice a data picture into ring slices. The pix_widthX is the image's x pixel length or subset length and the pix_widthY is the y pixel length or subset length (use a square image or subset image). The centerX and centerY parameters are the x and y coordinates where the analysis is centered. For a first time run through set perform_gaussian_analysis to false. This will stop the program after it creates a contour and radial image so you can verify if it is working till this point. Run:

```
python uniformity_analysis.py input_parameters.json
```

Look at the contour image to see whether the ring cuts and centering parameter you set are correct. Now look at the radial profile and identify Gaussian peaks you'd like to analyze for uniformity. Note the pixel where you'd like to start and end a Gaussian fit and put those in the gaussian_start_pixel and gaussian_end_pixel parameters. Try to make this span as wide as possible without overlapping other peaks that the radial plot reveals. Now you can set perform_gaussian_analysis to true and perform_slice_analysis to false and run the program with the exact command as before

```
python uniformity_analysis.py input_parameters.json
```

A Gaussian fit will be produced with the start and end pixels you specified and any background intensity that offsets the Gaussian from zero will be subtracted off. Play around with the start and end pixels for the fit if needed (this can alter results by fitting background noise to the Gaussian curve). If the fit looks good from here you can set perform_slice_analysis to true and the angle_slice to 45. Now run the program with the exact command as before.

```
python uniformity_analysis.py input_parameters.json
```

The program will produce a uniformity percentage in the terminal output and into an info.txt file. This will also produce a contour_slices image which is a visual interpretation of the uniformity analysis. For the visual interpretation of the analysis, see Fig. 3.4 caption.

You may now set the angle_slice parameter to lower values like 2 or 5 to increase the angular resolution of your image. This increases the time to run the analysis (there is room for the algorithms to be optimized).

4.4 Scale Customization and Other Parameters

There are many other parameters that you can control; please see the input_parameters_example.json file for explanations on each parameter. The code was originally designed for astronomical objects at milli-arcsec scales around 1 kilo-parsec away. If you do not know the angular size of a pixel set scaled to false and arcsec_per_pixel to 1 and everything will convert to pixels. Otherwise, adjust the scale to your needs with the parameters scale_factor and radius_from_source. If you don't know the distance set scaled to false, radius_from_source to 1 ignore the physical distances the program outputs. If you are working with milli-arcsec (which is what the example uses) you would set scale_factor to 1000 (base scale is arcsecs). The plot labels would need to be adjusted for other scales, along with the intensity scale if you are not using mJy/beam/area which is very specific to radio observations.

Chapter 5

Results

In this chapter, we present the spectral lines we measured and compare them to the lines observed 30 years previously. Then we show the images and plots that lead up to the uniformity calculations for six different locations in the OH maser shell of IRAS 03206+6521. There is a reference table for each piece of the shell that contributed to our results (see Tab. 5.1). For a summary of the uniformity results see Tables. 5.2 and 5.3. Lastly, we used these calculations to model the different parameter relationships, then we discuss other contributions from this work.

5.1 Spectral Lines

Our intent was to pick highly evolved sources that could be mapped out for stellar structure in the intermediate state as a spherical star is evolving into a planetary nebula. We provided high spectral resolution lines for two sources, which contributed to the knowledge collection of how OH/IR maser lines evolve or adapt to their environments through time. Our data collected during this study is the highest resolution ever used to record the spectral resolution of these sources since they started being observed 30 years ago (see Fig. 5.1).

IRAS 03206+6521 in 1986

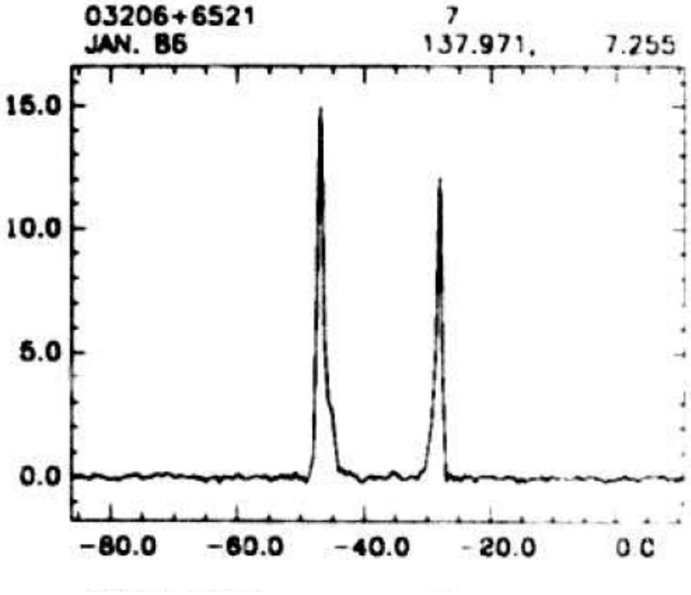

Figure 5.1 From Hekkert (1991) taken in January, 1986.

For IRAS 03206+6521 we detected a double-peaked spectrum (see Fig. 5.2) at the 1612 MHz OH line with the blue-shifted peak at 46.6 km/s with a flux of 5.1 Jy (see Fig. 5.2). This peak was the only one that measured strong enough to show Zeeman splitting between the right and left circularly polarized spectra. With the frequency peak separation of 1953.1250 Hz, we measure a magnetic field of 0.0698 +/- 0.034 μTesla. The red-shifted peak in this spectra at 28 km/s measured 0.5 Jy. Both peaks of this source were measured 30 years earlier (see Fig. 5.1) with single dish observations, and the peak fluxes were measured at much higher values (te Lintel Hekkert et al. 1991). Te Lintel Hekkert (1991) reports the flux of the blue-shifted and red-shifted peaks as 15 and 12 Jy respectively. It is not unusual to see a weaker line out of the two peaks or sometimes even just one line. The exact reasons for this are unknown but may relate to the mass loss processes. This drop in flux is probably due to two things: first, because of our higher resolution, our observations may have partially resolved the source's flux. This would mean that it was diffuse to begin with. Second, the evolution of the maser shells became more diffuse as they evolved over time. The red-shifted peak shows evidence of more rapid diffusion than that of the blue-shifted peak in that: it is very weak at our resolution, and not as comparatively strong as it has been in the past. Our images also show a diffuse region on the redshifted side of the OH maser shell (although still uniform) which helps explain the large difference in maser line flux from the blue-shifted side (see Fig. 5.23).

In IRAS 03293+6010 we detected only a single OH 1612 MHz peak of the maser shell, likely indicating that the uniformity of the mass loss is not spherical and is affecting the geometry of the shell by a large percentage. We were not able to map the source even when attempting to map it at lower resolutions.

The spectra of IRAS 03293+6010 has its blue-shifted peak at -68.5 km/s at 1.82 Jy (see Fig. 5.4). The red-shifted peak was not detected by us, although it has been previously detected (te Lintel Hekkert et al. 1991) by single dish observations at 2.1 Jy. Not detecting the red-shifted peak hints that the red-shifted peak has either been quite diffuse for some time or that it has recently become diffuse.

Observing masers in these sources reveals the specific temperature (-450 K) and density (number densities $\sim 10^7$) conditions in these OH maser shells. Masers are very sensitive to conditions. In the region where we do not see masers we know that they are simply not masing along our line of sight. The masers we do see here and in the images in this chapter may even be stronger at different viewpoints, but most of our detections lie at high Doppler-shifts indicating they are moving directly toward or away from us, and we likely view their full strength because of the direction they are travelling.

Water maser lines were not detected in any of our sources, indicating that there currently is not the highly compacted masing water shell that we expected to observe in some of our sources. Being unable to detect (down to a couple of mJy) H_2O supports that these stars are highly evolved. Water masers are sensitive to temperature and density and since we did not detect them we know certain conditions are not being met along our line of sight. The most likely scenario is the density of H_2O is low near the star because strong radiation fields have carried the majority of H_2O molecules to far distances. Lewis (1989) pieced a chronology of OH/IR star evolution through detecting the presence or lack of particular masers. In this chronology, the lack of water masers marks a late stage for sources having exhibited 1612 MHz masers at some point. Having the 1612 MHz OH line without the 22 GHz H_2O and other OH main lines (1665 MHz and 1667 MHz) marks either the 7th or 8th stage for IRAS 03206+6521 and IRAS 03293+6010 (stage 11 indicating a planetary nebula). Water masers have been seen in rare cases in planetary nebulae, but are suspected to only last for less than 100 years (Gómez 2007).

In IRAS 21554+6204 and IRAS 22177+5936 we observed them to have no OH lines in our direction down to 0.1 mJy sensitivity and thus they could not be mapped. The presence of no OH lines marks either the planetary nebula stage or a highly diffuse maser environment which would be better suited for lower resolution observations to confirm detections. As the OH circumstellar shell expands, eventually the density and temperature drop to levels that can no longer support masers. Alternatively, this might be due to natural maser line variability in which the lines might have become extremely weak. Variability in maser lines has been observed on the order of months, a fairly quick timescale for an astronomical phenomenon (Sugiyama et al. 2017).

Two of our sources (IRAS 01304+6211 and IRAS 05073+5248) were observed at non-ideal times and the data was not usable. They potentially could have been observed overhead of the VLBA, but were scheduled and observed close to the horizon and therefore lack the desired UV coverage for the best imaging. Phase referencing failed with this setup to apply needed calibration due to the phase calibrators being very weak. Due to this, we do not claim our non-detection of the maser lines searched for in these sources to be evidence to support any conclusion.

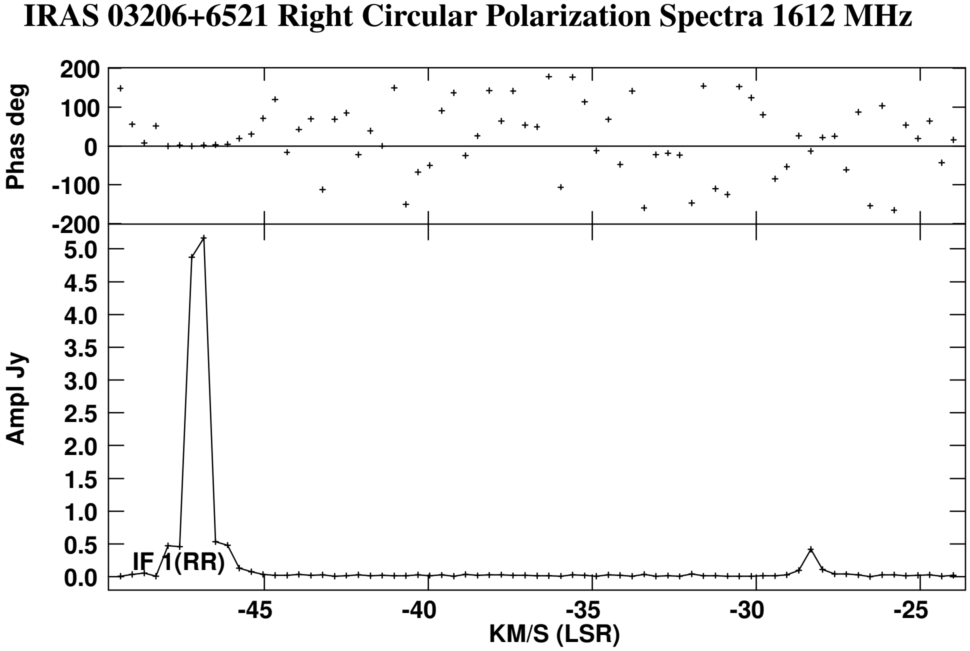

Figure 5.2 Spectral line plot for IRAS 03206+6521 with right circular polarization. Intensity (Jy) vs LSR velocity (km/s) (bottom). Phase (degrees) vs LSR velocity (km/s) (top). The blue-shifted peak (left side) has a value around 5.2 Jy and an image of this peak is in Fig. 5.3. The red-shifted peak has a value around 0.5 Jy and an image of this is in Fig. 5.23.

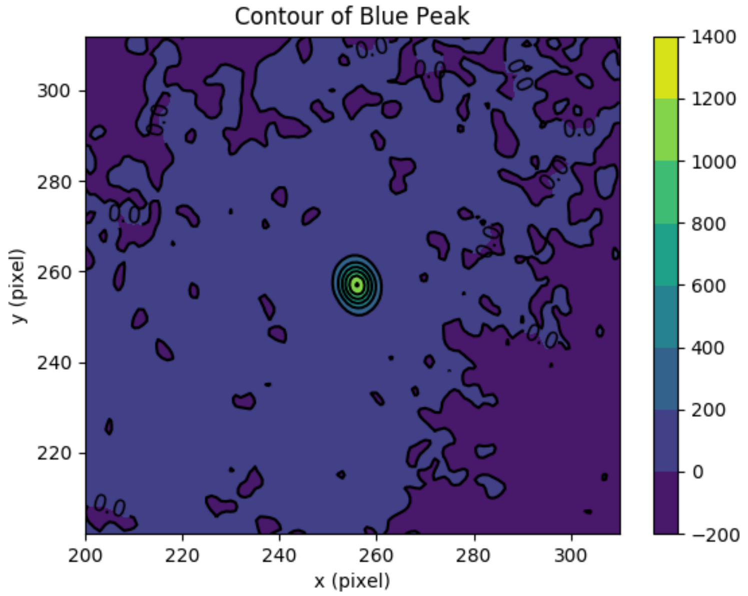

Figure 5.3 The contour image of the blue shifted peak. Velocity -8.7 km/s (star's reference frame). Pixel scale: 1 pixel is 1.2 arcsec. Intensities are in millijansky.

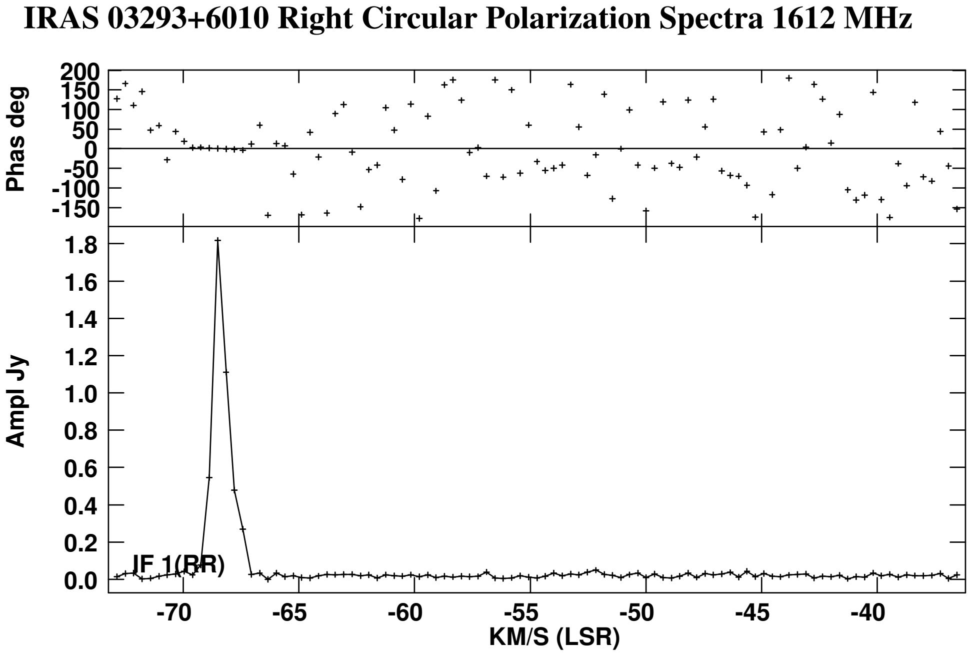

Figure 5.4 Spectral line plot for IRAS 03293+6010 with right circular polarization. Intensity (Jy) vs LSR velocity (km/s) (bottom). Phase (degrees) vs LSR velocity (km/s) (top). The blue-shifted peak has a value around 1.8 Jy while the red-shifted peak is not seen.

5.2 Intensity Maps of IRAS 03206+6521

We mapped out the 1612 MHz emission IRAS 03206+6521 at high resolution at several distinct Doppler-shifted velocities. This allowed us to peer deep into several layers of the circumstellar maser shell of this OH/IR star (see Tab. 5.1). We found many maser features in partially filled shells. We analyzed these shells for uniformity, thickness, and radial shell location.

Table 5.1 Figure References for IRAS 03206+6521

Region Around Star	Image	Radial Profile	Gaussian Fit	Uniformity Plot
blue shell	Fig. 5.5	Fig. 5.6	Fig. 5.7	Fig. 5.8
red shell	Fig. 3.1	Fig. 3.2	Fig. 3.3	Fig. 3.4
blue inner	Fig. 5.19	Fig. 5.20	-	-
blue arc	Fig. 5.15	Fig. 5.16	Fig. 5.17	Fig. 5.18
red peak shell	Fig. 5.23	Fig. 5.24	Fig. 5.25	Fig. 5.26
blue peak (far)	Fig. 5.9	Fig. 5.10	Fig. 5.12	Fig. 5.13
blue peak (close)	Fig. 5.9	Fig. 5.10	Fig. 5.11	Fig. 5.14
red inner	Fig. 5.21	Fig. 5.22	-	-

5.2.1 Region: Blue Shell

This analysis was done by averaging 12 images (regions moving -7.3 km/s to -10.5 km/s away from the central star). This represents the blue Doppler-shifted spectral peak or extreme blue-shifted 1612 MHz OH maser shell. The strong spectral line of the line profile which occupies the center of the images was masked out to study the weak uniform pieces of the maser shell (see Fig. 5.5). In this image, one can see a maser spot in the lower left. When the radial profile of this region was measured (see Fig. 5.6) a notable Gaussian looking feature was visible at 120 mas (pixel 100). This corresponds to a visible maser spot in the contour image. A Gaussian was fit to a portion of the radial profile (see Fig. 5.7). A 3.1 sigma detection was made for this shell that is located 100 pixels from the center. The fit to the shell gives a distance of $3.86*10^{16}$ cm from the star and a shell thickness of $0.078*10^{16}$ cm. The uniformity analysis indicates that this shell is 19.4% uniform (see Fig. 5.8). Seeing this maser shell here indicates the mass loss processes are non-uniform because this shell is showing up at a location inconsistent with its velocity, assuming uniform mass loss. Its velocity is actually too high (probably a more recent ejection from the star) for its location compared to the stronger portion of the shell or the central feature shown earlier (see Fig. 5.3).

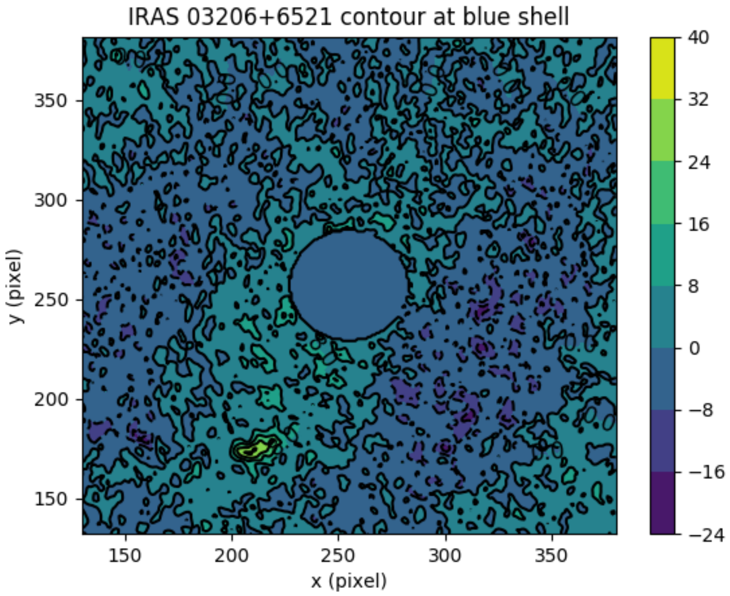

Figure 5.5 Color contour intensity map of IRAS 03206+6521 centered on the IRAS source at 1612MHz of the blue shell region. The image center is masked out due to its high brightness so that weaker features can be seen. A maser spot can be seen in the lower left, appearing at a location indicative of non-uniform expansion. This maser fills a small part of a circular shell at its location. Velocity -8.7 km/s (star's reference frame). Pixel scale: 1 pixel is 1.2 arcsec. Intensities are in millijansky.

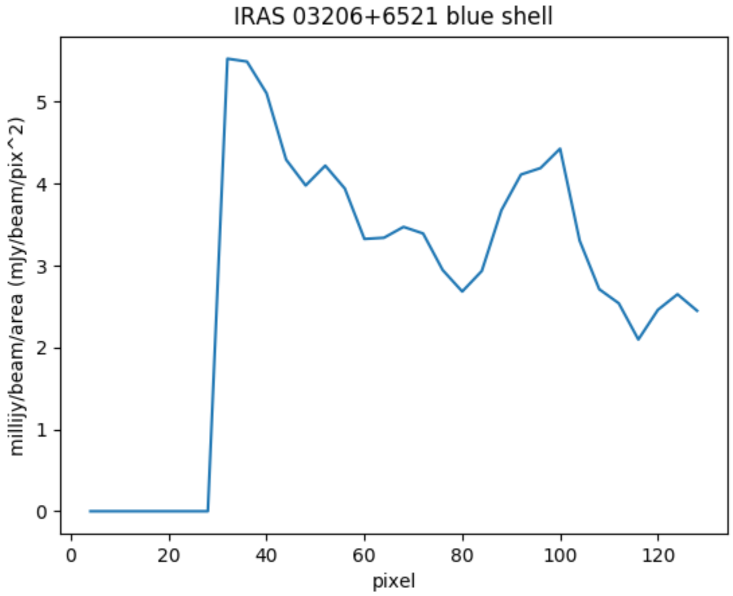

Figure 5.6 Radial plot of the 1612 MHz emission of IRAS 03206+6521 of the blue shell region. The center area (0 - 30 pixels) is masked out due to a strong maser feature. The Gaussian-like feature at around pixel 100 was visually identified and fitted to a Gaussian in the following figure. Intensity in concentric rings is totaled then divided by the total area within the ring.

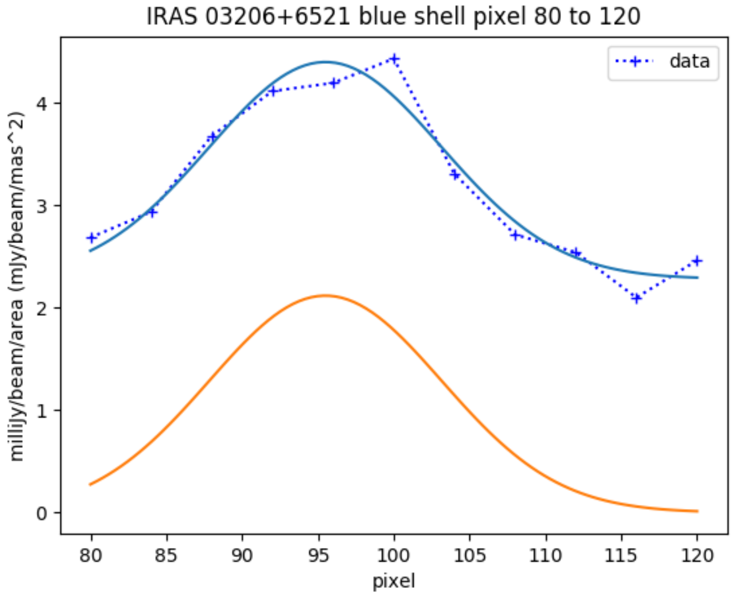

Figure 5.7 Gaussian fit to a particular radial range of the radial plot IRAS 03206+6521 of the blue shell region. Blue plus signs represent the data points. Dotted blue lines are a linear interpolation between data points. The solid blue line is the fit. The solid orange line is the fit with which the continuum or offset above zero was subtracted.

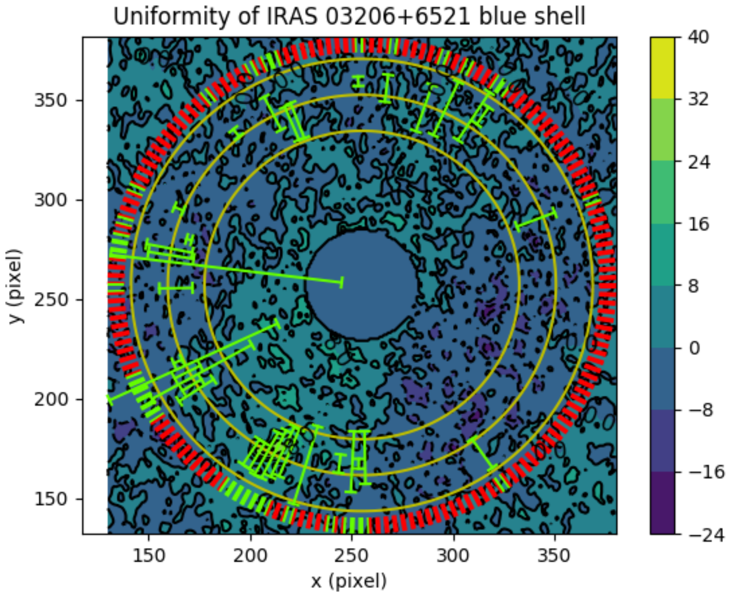

Figure 5.8 Gaussian fits to IRAS 03206+6521 were overlaid on the intensity map to show the uniformity of the blue shell region at velocity -8.7 km/s (star's reference frame). See Figure 3.4 for more details. This maser shell showed a uniformity of 19.4%. Pixel scale: 1 pixel is 1.2 arcsec. Intensities are in millijansky.

5.2.2 Region: Blue Peak Shell

This region represents the peak of the blue Doppler-shifted spectral line or cap of the blue-shifted 1612 MHz OH maser shell (-8.7 km/s in the star's frame of reference). The central main feature is masked so that detail can be extracted from the non-uniform portions of the image. In the contour image (see Fig. 5.9) two maser spots can be seen (one lower left and one slightly low and slightly left of the image center). The radial profile (see Fig. 5.10) picked up the two features at pixel 50 and pixel 100. Two Gaussians were fit to this radial profile (see Fig. 5.12 and Fig. 5.11). A 3.1 sigma detection was made for the first shell that is located 50 pixels from the center and a 3.3 sigma detection was made for the second shell located 100 pixels from the center. The fit to the inner shell gives a distance of $3.94{*}10^{16}$ cm from the star and a shell thickness of $0.062{*}10^{16}$ cm. The uniformity analysis indicates that this shell is 25.0% uniform (see Fig. 5.13). The fit to the outer shell gives a distance of $3.94*10^{16}$ cm from the star and a shell thickness of $0.032*10^{16}$ cm. The uniformity analysis indicates that this shell is 11.1% uniform (see Fig. 5.14). These two shells are separated by a distance of $0.209*10^{16}$ cm but are approximately the same distance from the star. Interestingly, the Gaussian peaks are about the same height but the uniformity is different. The outer shell is less uniform, and this is what we would expect, but it is not much farther than the inner shell. In general, we expect that as the shell layers are pushed outward, more non-uniformity would be the trend.

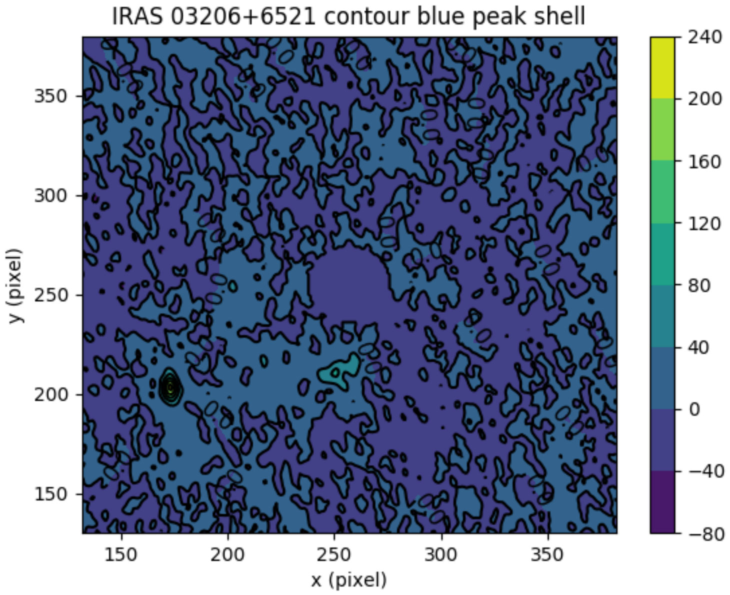

Figure 5.9 Color contour intensity map of IRAS 03206+6521 centered on the IRAS source at 1612MHz of the blue peak region. Velocity -8.7 km/s (star's reference frame). Pixel scale: 1 pixel is 1.2 arcsec. Intensities are in millijansky.

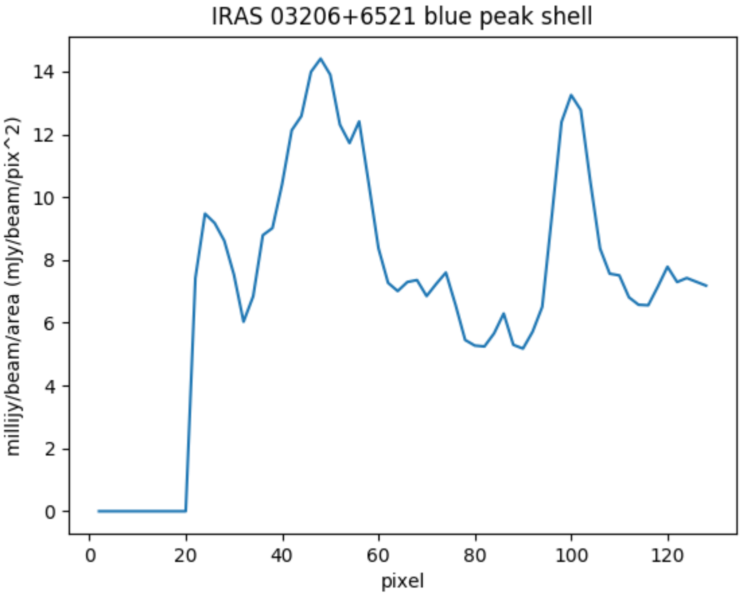

Figure 5.10 Radial plot of the 1612 MHz emission of IRAS 03206+6521 of the blue peak region. Intensity in concentric rings is totaled then divided by the total area within the ring. We fit two peaks from image corresponding to the blue-shifted spectral line peak and denoted them as "close" (pixel 50) and "far" (pixel 100).

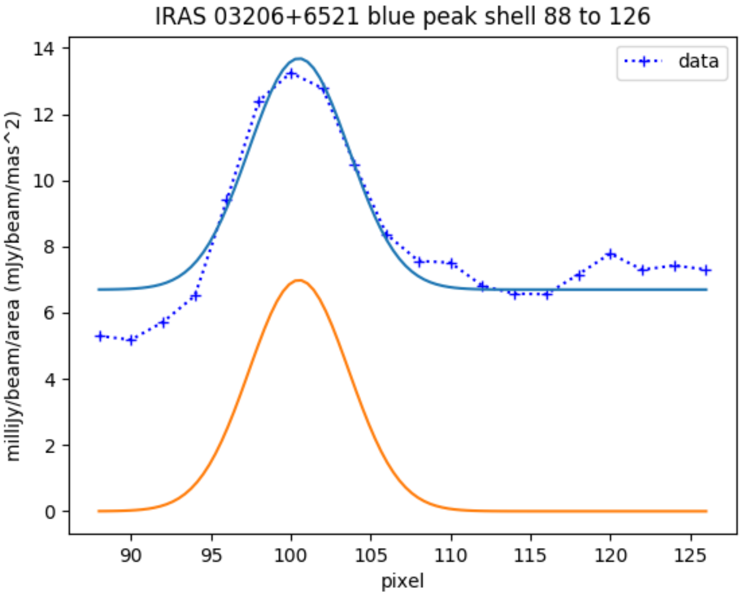

Figure 5.11 Gaussian fit to the far peak of the radial plot IRAS 03206+6521 of the blue peak far region. Blue plus signs represent the data points. Dotted blue lines are a linear interpolation between data points. The solid blue line is the fit. The solid orange line is the fit with which the continuum or offset above zero was subtracted.

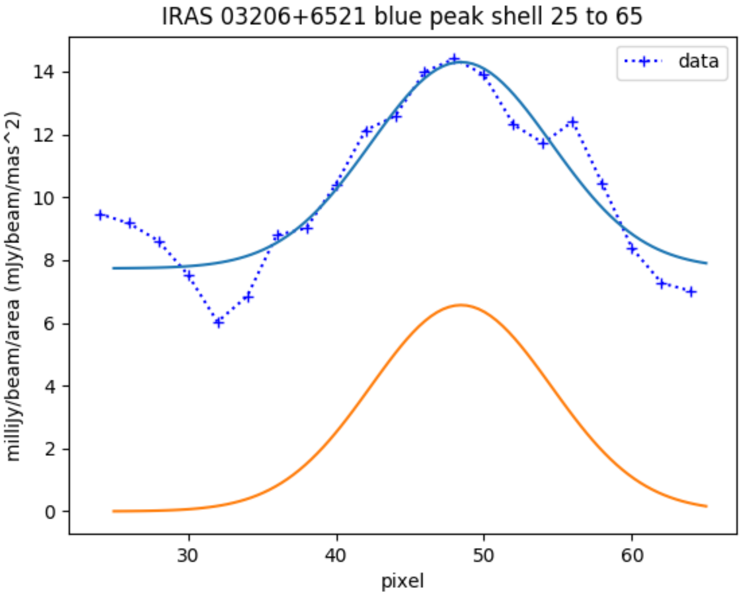

Figure 5.12 Gaussian fit to the closer peak of the radial plot IRAS 03206+6521 of the blue peak close region. Blue plus signs represent the data points. Dotted blue lines are a linear interpolation between data points. The solid blue line is the fit. The solid orange line is the fit with which the continuum or offset above zero was subtracted.

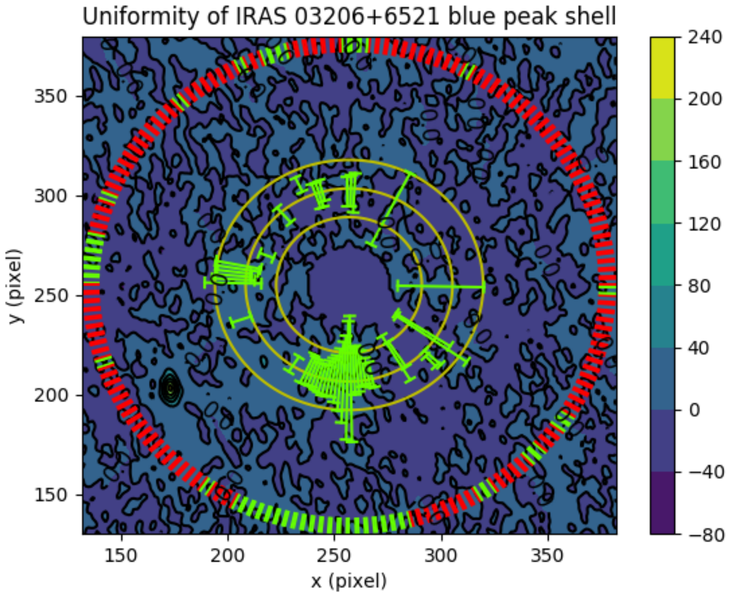

Figure 5.13 Gaussian fits to IRAS 03206+6521 were overlaid on the intensity map to show the uniformity of the blue peak shell close region at velocity -8.7 km/s (star's reference frame). See Figure 3.4 for more details. This maser shell showed a uniformity of 25.0%. Pixel scale: 1 pixel is 1.2 arcsec. Intensities are in millijansky.

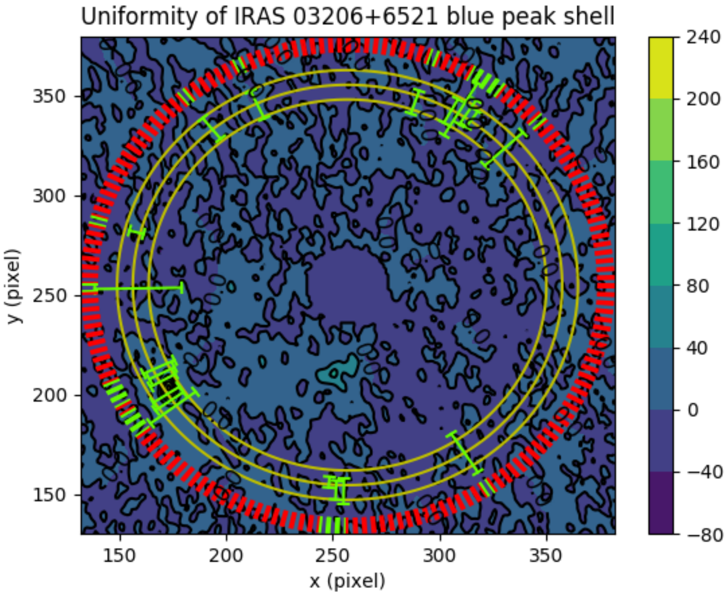

Figure 5.14 Gaussian fits to IRAS 03206+6521 were overlaid on the intensity map to show the uniformity of the blue peak shell far region at velocity -8.7 km/s (star's reference frame). See Figure 3.4 for more details. This maser shell showed the least degree of uniformity at 11.0%. Pixel scale: 1 pixel is 1.2 arcsec. Intensities are in millijansky.

5.2.3 Region: Blue Arc

This represents a piece of the 1612 MHz OH maser shell that is a side lobe of the strong blue Doppler-shifted peak at a velocity (-8.4 km/s in the star's frame of reference) slightly lower than the peak velocity, believed to be an outer layer that has slowed slightly (see Fig. 5.15). In this image, one can see a maser spot in the lower left, which corresponds to that of the blue shell (see Fig. 5.5). When the radial profile of this region was calculated (see Fig. 5.16) a notable Gaussian looking feature was visible at 164 mas (pixel 137) where you can see the arc-like feature in the contour image. A Gaussian was fit to a portion of the radial profile (see Fig. 5.17). An 8.5 sigma detection was made for this shell that is located 137 pixels from the center. The fit to the shell gives a distance of $4.39{*}10^{16}$ cm from the star and a shell thickness of $0.054{*}10^{16}$ cm. The uniformity analysis indicates that this shell is 15.0% uniform (see Fig. 5.18). The shell that was measured from this image is the furthest shell measurement we have in our data. This also shows the most visually connected shell structure, even though it is quite thin. The masers likely can't support themselves for long due to this thin layer expanding. We suspect density will soon drop (density has already dropped in up to 75% of the shell) below the conditions required for masers.

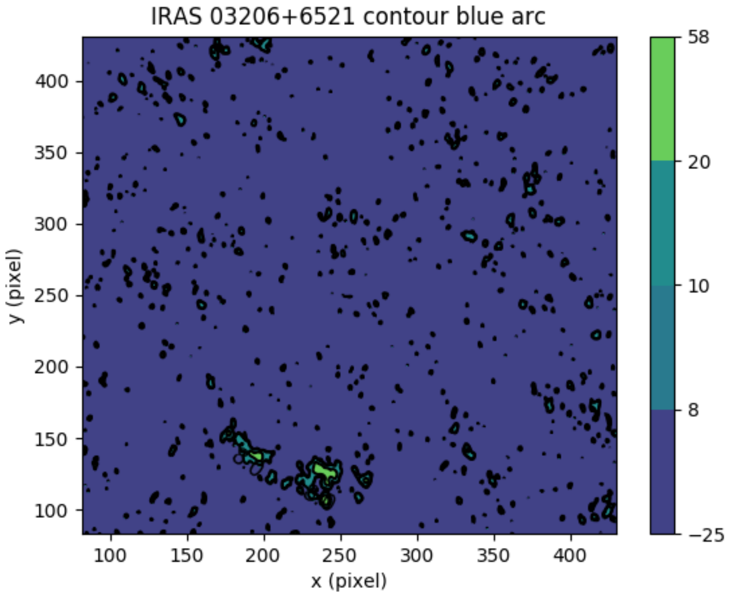

Figure 5.15 Color contour intensity map of IRAS 03206+6521 centered on the IRAS source at 1612MHz of the blue arc region. Velocity -7.6 km/s (star's reference frame). Pixel scale: 1 pixel is 1.2 arcsec. Intensities are in millijansky. The 1612 MHz masers are in the bottom left.

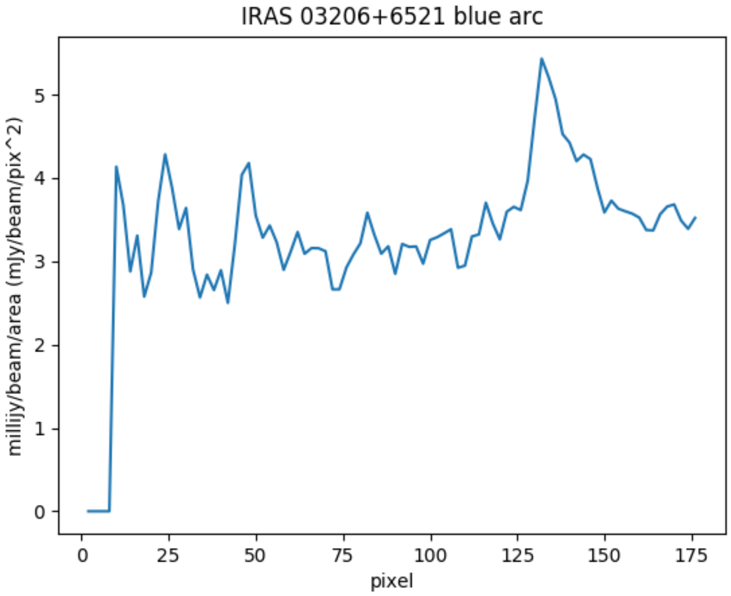

Figure 5.16 Radial plot of the 1612 MHz emission of IRAS 03206+6521 of the blue arc region. Intensity in concentric rings is totaled then divided by the total area within the ring. We fit a Gaussian to the peak pixel 137.

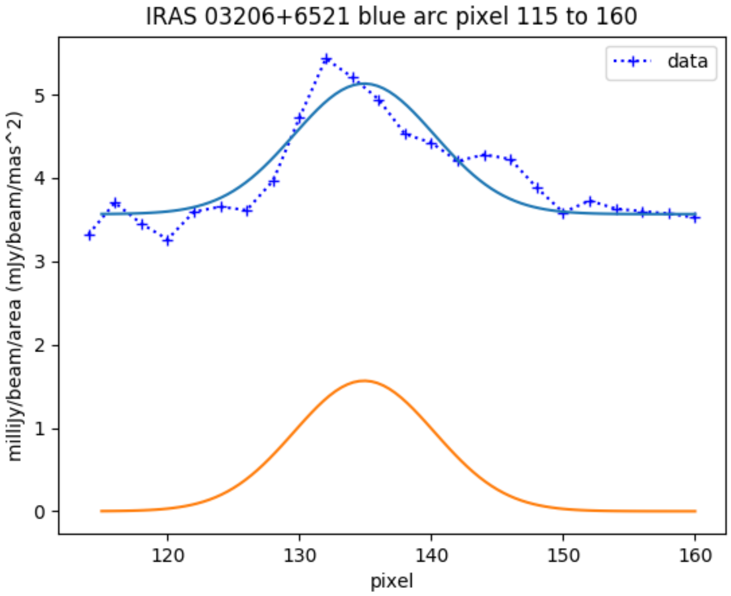

Figure 5.17 Gaussian fit to a particular radial range of the radial plot IRAS 03206+6521 of the blue arc region. Blue plus signs represent the data points. Dotted blue lines are a linear interpolation between data points. The solid blue line is the fit. The solid orange line is the fit with which the continuum or offset above zero was subtracted.

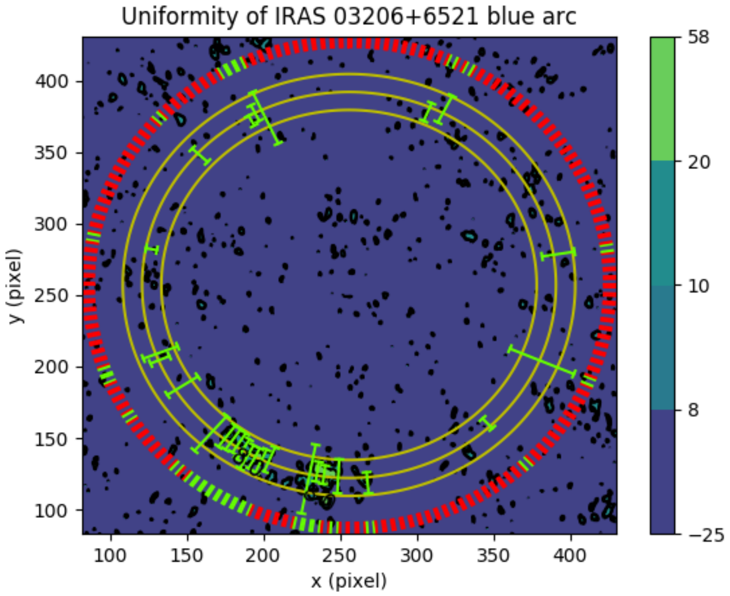

Figure 5.18 Gaussian fits to IRAS 03206+6521 were overlaid on the intensity map to show the uniformity of the blue arc region at velocity -7.6 km/s (star's reference frame). See Figure 3.4 for more details. This maser shell showed a uniformity of 15.0%. Pixel scale: 1 pixel is 1.2 arcsec. Intensities are in millijansky.

5.2.4 Region: Blue Inner

No Gaussian peaks could be fit for the inner blue-shifted portions of the OH maser shell (0 km/s to -7.3 km/s in the star's frame of reference). This is the piece of the shell beyond the blue-shifted peak shell where the material is generally pushed tangent and slightly toward our direction. We had hoped to see structure here but knew that the viewpoint for masers is less desirable because the medium is mostly expanding tangent to our direction. It is likely that there are masers in this region of the shell and that a certain degree of symmetry in these regions still holds. In the image (see Fig. 5.19) we see noise, and when we analyze the radial plot (see Fig. 5.20) no Gaussians could be fit.

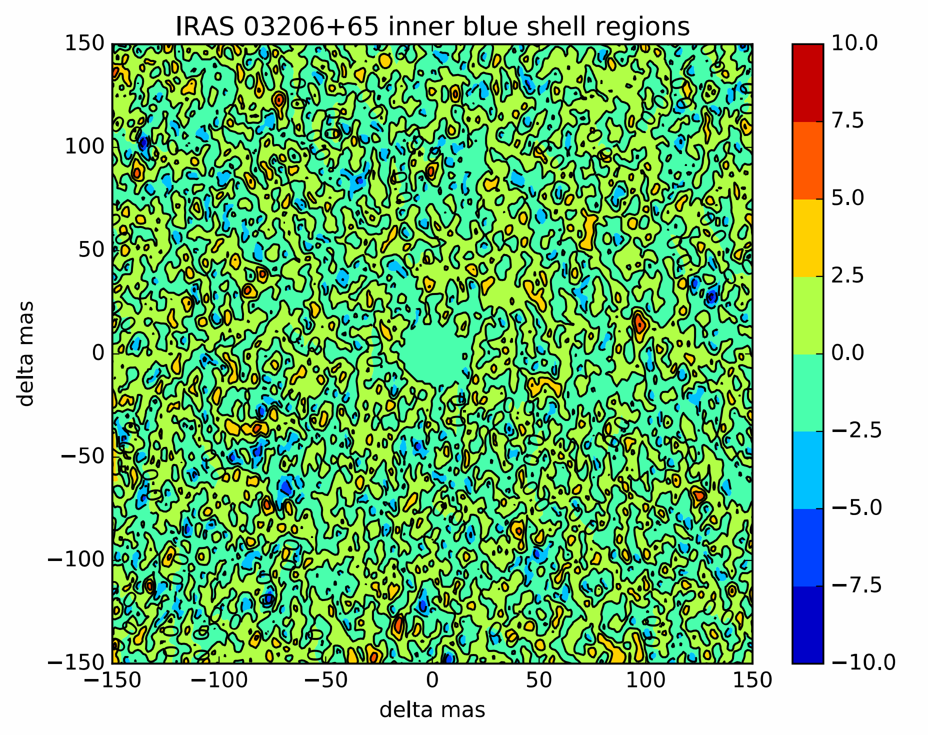

Figure 5.19 Color contour intensity map of IRAS 03206+6521 centered on the IRAS source at 1612MHz of the blue inner region. Pixel scale: 1 pixel is 1.2 arcsec. Intensities are in millijansky.

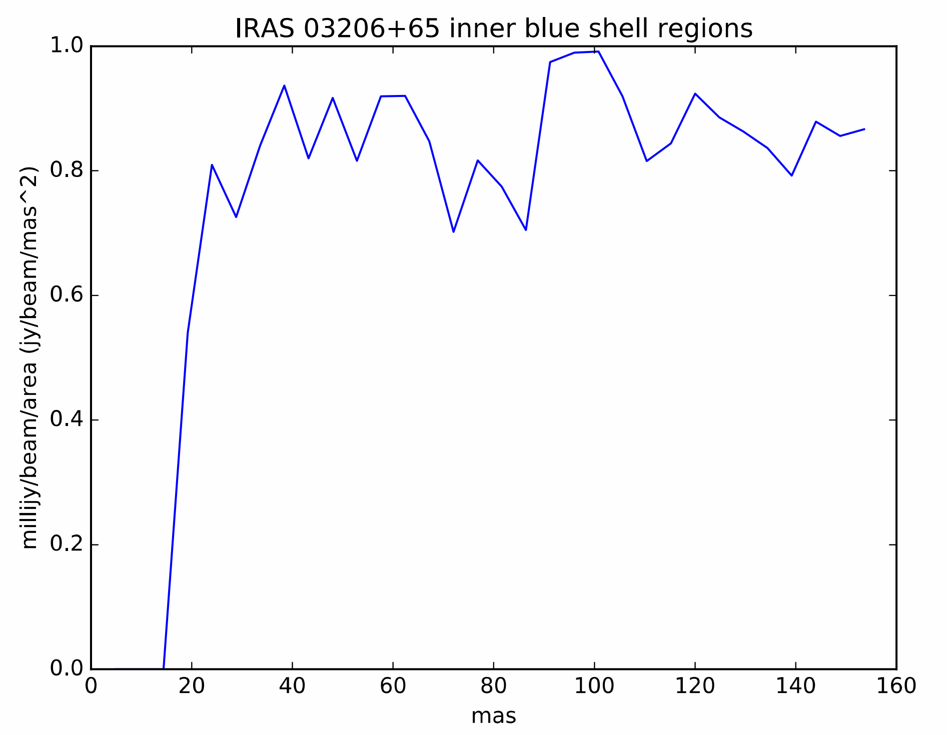

Figure 5.20 Radial plot of the 1612 MHz emission of IRAS 03206+6521 of the blue inner region. Intensity in concentric rings is totaled then divided by the total area within the ring. There was no Gaussian fit to any features in the inner portion of the blue shell.

5.2.5 Region: Red Inner

The inner red-shifted images were averaged (0 km/s to 8.3 km/s in the star's frame of reference). These would be the portions of the shell beyond the halfway mark, representing material that is moving mostly tangent but slightly red-shifted from our direction. No strong Gaussian peaks could be identified from the image (see Fig. 5.21) and the radial plot (see Fig. 5.22). The results of this region were the same as the inner blue region for likely the same reason, the tangent viewpoint makes masers difficult to detect.

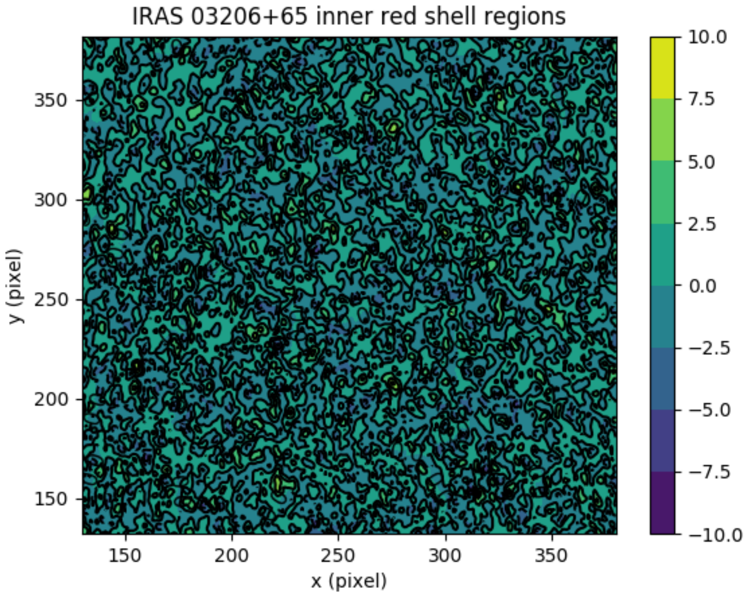

Figure 5.21 Color contour intensity map of IRAS 03206+6521 centered on the IRAS source at 1612MHz of the red inner region. Velocity 8.3 km/s (star's reference frame). Pixel scale: 1 pixel is 1.2 arcsec. Intensities are in millijansky.

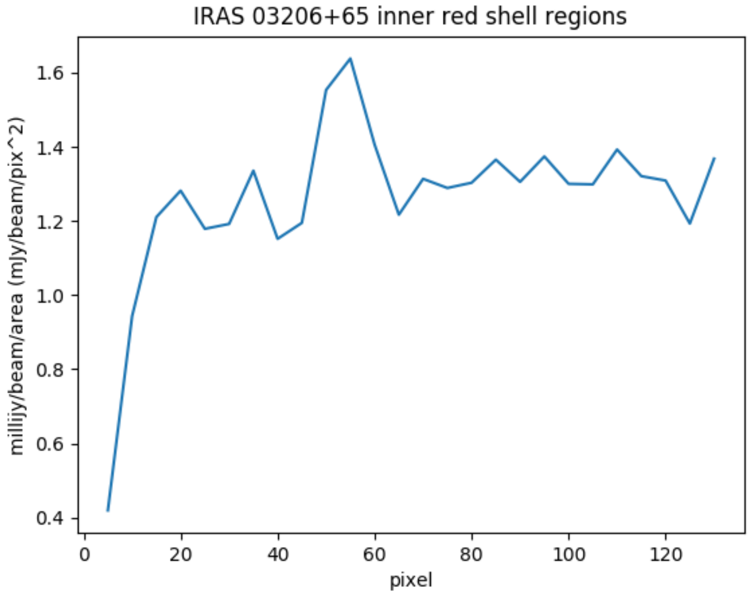

Figure 5.22 Radial plot of the 1612 MHz emission of IRAS 03206+6521 of the red inner region. Intensity in concentric rings is totaled then divided by the total area within the ring.

5.2.6 Region: Red Peak Shell

This region represents the peak image of the red-shifted shell (9.8 km/s in the star's frame of reference). The image (see Fig. 5.23) shows a very diffuse looking picture. There are three main central peaks that contributed to this 1612 MHz maser shell. The location of the star in this image (pixel 252, 263) is slightly below the left feature. Upon examining the radial profile (see Fig. 5.24) a very clear Gaussian peak showed up at 12 mas (pixel 10). A Gaussian was fit to a portion of the radial profile (see Fig. 5.25). A 79 sigma detection was made for this shell that is located 10 pixels from the center. The fit to the shell gives a distance of $3.49 * 10^{16}$ cm from the star and a shell thickness of $0.087 * 10^{16}$ cm. The uniformity analysis indicates that this shell is 85.0% uniform (see Fig. 5.26), and is the thickest shell measured. Even though the portions to the bottom right of the star are relatively weak, many of the small angular portions are fit to Gaussians. This is one of the closest measurements we have to the star. It contrasts that of the blue arc region which is thin and mostly non-uniform.

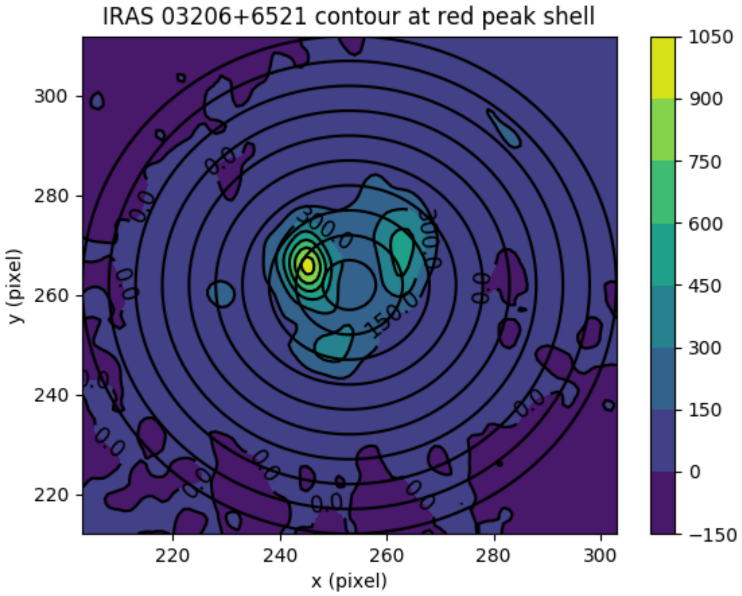

Figure 5.23 Color contour intensity map of IRAS 03206+6521 centered on the IRAS source at 1612MHz of the red peak region. Velocity 9.8 km/s (star's reference frame). Pixel scale: 1 pixel is 1.2 arcsec. Intensities are in millijansky.

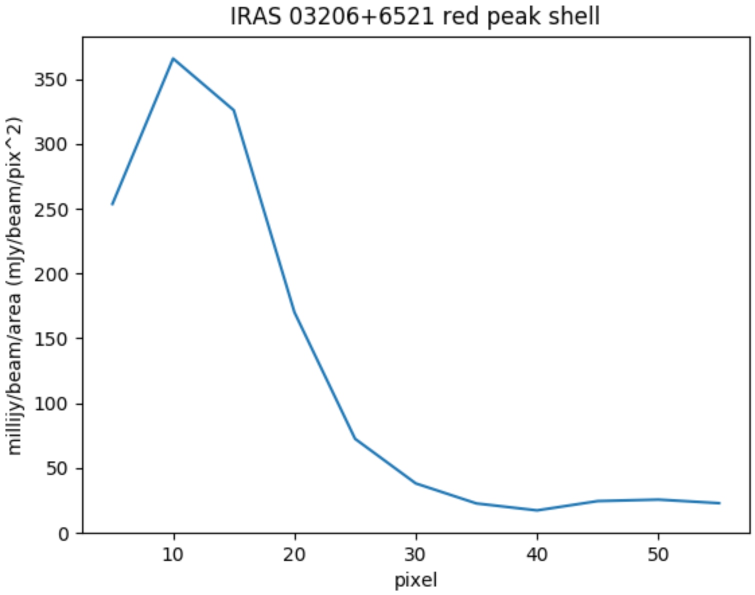

Figure 5.24 Radial plot of the 1612 MHz emission of IRAS 03206+6521 of the red peak region. Intensity in concentric rings is totaled then divided by the total area within the ring. A Gaussian was fitted centered on pixel 15

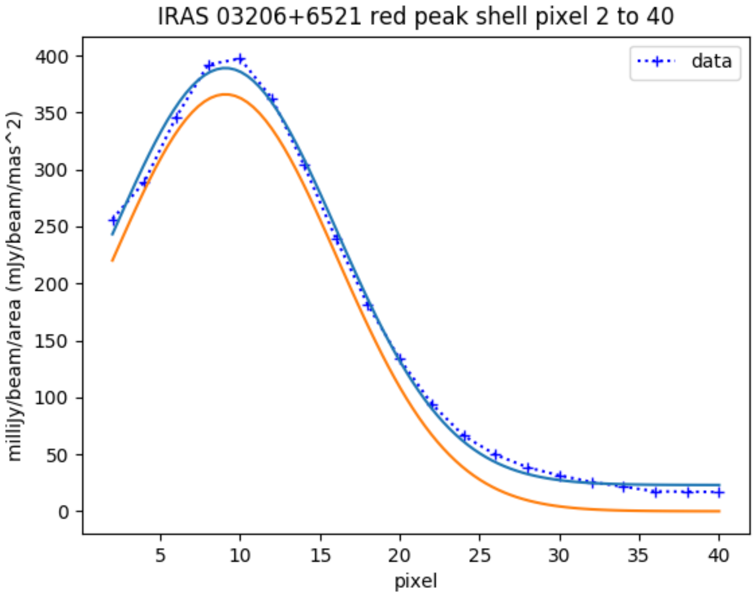

Figure 5.25 Gaussian fit to a particular radial range of the radial plot IRAS 03206+6521 of the red peak region. Blue plus signs represent the data points. Dotted blue lines are a linear interpolation between data points. The solid blue line is the fit. The solid orange line is the fit with which the continuum or offset above zero was subtracted.

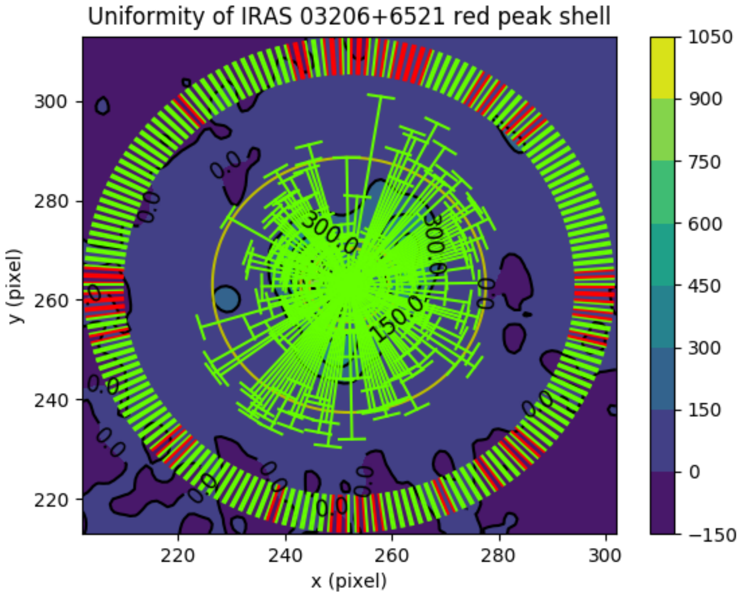

Figure 5.26 Gaussian fits to IRAS 03206+6521 were overlaid on the intensity map to show the uniformity of the red peak shell region at velocity 9.8 km/s (star's reference frame). See Figure 3.4 for more details. This maser shell showed a uniformity of 85% which was the highest degree of uniformity measured. Pixel scale: 1 pixel is 1.2 arcsec. Intensities are in millijansky.

5.2.7 Region: Red Shell

This region represents the farthest portions of the shell from us. This analysis was done by averaging seven images (at -8.7 km/s to -10.5 km/s in the star's frame of reference) to represent the extreme red Doppler-shifted portion of the 1612 MHz maser shell. The image (see Fig. 3.1) looks similar to the red peak shell because it involves that image, but the analysis does differ. The radial profile (see Fig. 3.2) displays one main peak. A Gaussian was fit to a portion of the radial profile (see Fig. 3.3). A 50 sigma detection was made for this shell that is located 10 pixels from the center. The fit to the shell gives a distance of $3.56 * 10^{16}$ cm from the star and a shell thickness of $0.066 * 10^{16}$ cm. The uniformity analysis indicates that this shell is 60.6% uniform (see Fig. 3.4), but an environment that looks like it is becoming diffuse. The portion to the bottom right of the star is weak, many of the small angular portions are fit to Gaussians in contrast to that of the red peak shell.

5.3 Uniformity of the OH Maser Shell

We are the first to quantify the uniformity of an OH/IR circumstellar OH maser shell at 1612 MHz. We did this by studying nearby highly evolved OH/IR stars on the verge of becoming planetary nebulae. Whether an OH/IR star was on the verge of becoming a planetary nebula was hinted at by the high mass loss rate and the dust factor. For more information on how this was measured see section 3.1.

The high-resolution maps of IRAS 03206+6521 reveal its maser shell morphology and uniformity at this very late evolutionary stage (see Tab. 5.1). We were able to find a specific uniformity measurement from 11% to 85% at six locations in the OH maser shell (see Tab. 5.2). The fit (see Fig. 5.28) indicates that the mass loss in this star was non-uniform before the OH maser shell. A small extrapolation gives 100% uniformity at $3.43*10^{16}$ cm. We suspect that this distance could represent the photodissociation zone (where H_2O separates into the H and OH ions). If so, it is likely that magnetic fields play a role in shaping the mass loss through the OH shell because magnetic fields accelerate, moving charged particles like the OH ion in this case.

Table 5.2 Physical Uniformity Measurements. Distance is the off axis radial distance

Off-Axis Radial Distance (cm)	Radial Distance (cm)	Uniformity Percentage	Thickness (cm)	Source of Measurement
$0.053\text{x}10^{16}$	$3.56\text{x}10^{16}$	60.6%	$0.066\text{x}10^{16}$	red shell
$0.581\text{x}10^{16}$	$4.39\text{x}10^{16}$	15.0%	$0.054\text{x}10^{16}$	blue arc
$0.411\text{x}10^{16}$	$3.86\text{x}10^{16}$	19.4%	$0.078\text{x}10^{16}$	blue shell
$0.209\text{x}10^{16}$	$3.94\text{x}10^{16}$	25.0%	$0.062\text{x}10^{16}$	blue peak (close)
$0.433\text{x}10^{16}$	$3.94\text{x}10^{16}$	11.1%	$0.032\text{x}10^{16}$	blue peak (far)
$0.045\text{x}10^{16}$	$3.49\text{x}10^{16}$	85.0%	$0.087\text{x}10^{16}$	red peak

Table 5.3 Angular Uniformity Measurements. Distance is the off axis radial distance

Off-Axis Radial Distance (mas)	Uniformity Percentage	Thickness (mas)	Source of Measurement
14.75	60.6%	18.411	red shell
161.89	15.0%	15.071	blue arc
114.60	19.4%	21.680	blue shell
58.14	25.0%	17.221	blue peak (close)
120.62	11.1%	8.851	blue peak (far)
12.65	85.0%	24.180	red peak

5.4 Fitting Maser Shell Relationships

Using our measurements in the OH maser shell, we came up with useful parameter relationships to constrain mass loss models. These relationships include: uniformity versus radial distance, uniformity versus thickness, mass loss rates $*$ uniformity versus radial distance, and mass loss rates $*$ uniformity versus thickness. These relations are a key contribution to understanding late stages of stellar evolution and provide a basic non-spherical model for OH/IR star morphology based off of high-resolution observations.

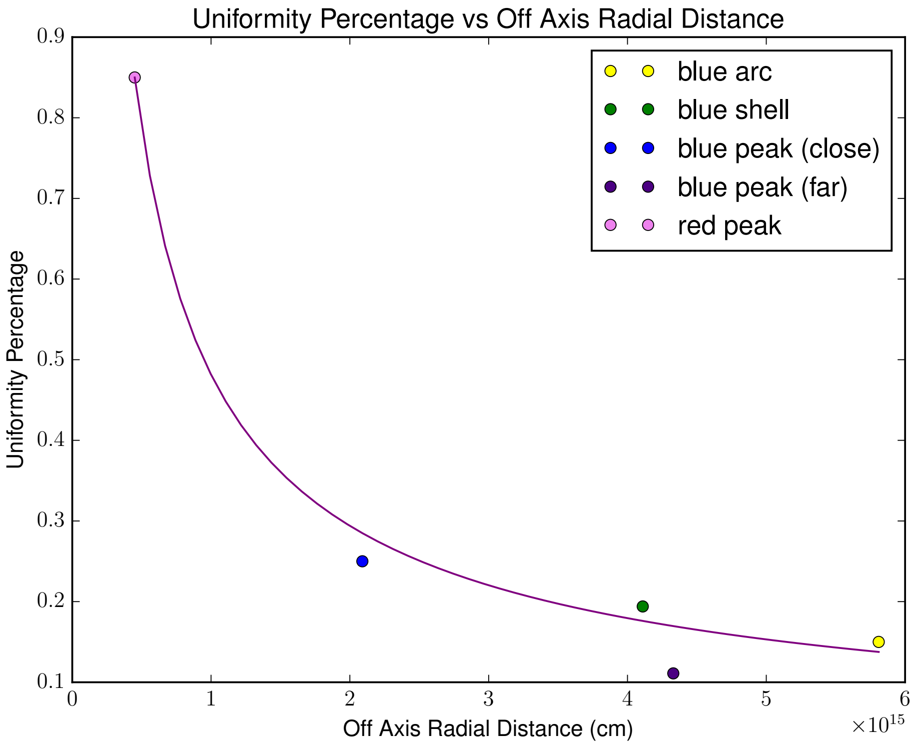

Figure 5.27 How uniform the 1612 MHz maser shell is as a function of off-axis radius. The points were weighted according to their detection Gaussian strength above the noise. The regions in the legend are data points from specific regions in the OH maser shell. In the regions where we find the peak of the blue-shifted spectral line we found 2 different maser shells at different radial locations and denote them "close" and "far" with respect to the center of the image.

The power law fit in equation (5.1) shows the percentage of uniformity as a function of off-axis distance (see Fig. 5.27). The points were weighted according to their detected Gaussian strength above the noise. Off-axis distance refers to a two-dimensional distance measured directly from an image (x-y plane or face on view) that doesn't include z-axis. The fit parameters for the power law are:

$$p = 0.093 * r^{-0.71} \tag{5.1}$$

where p is the percentage of uniformity and r is the off-axis radial distance from the star in 10^{16}

cm.

This reveals at what off-axis radial distance we begin to observe deviations from spherical uniformity for IRAS 03206+6521. We expect that at some point we would observe deviations from spherical symmetry, and we do see it here. Interestingly enough, we observed a drastic drop (74%) in uniformity through the whole OH maser shell. This finding puts constraints on how mass loss models for OH/IR stars need to account for a certain amount of non-uniformity through the OH maser shell.

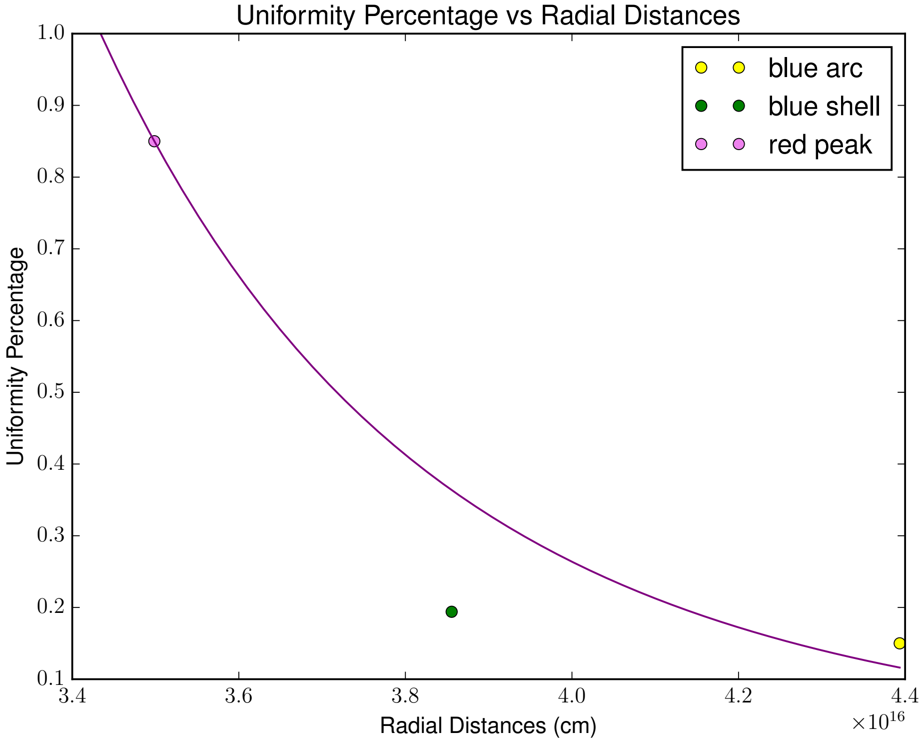

Figure 5.28 How uniform the 1612 MHz maser shell is as a function of radius. The points were weighted according to their detection Gaussian strength above the noise. The regions in the legend are data points from specific regions in the OH maser shell.

At this point, we developed a relationship for velocity and z-axis distance (see section 3.1) and estimated three-dimensional distances to maser shells. A power law fit didn't converge with strongly weighted points having nearly the same radial distance so we kept the strongest point at each major radial distance. The percentage of uniformity was plotted as a function of radial distance (see Fig. 5.28) and a power law was fit to the data (see equation (5.2)). The points were weighted according to their detected Gaussian strength above the noise. The fit parameters for the power law are:

$$p = 47916 * r^{-8.73} \tag{5.2}$$

where p is the percentage of uniformity and r is the radial distance from the star in 10^{16} cm.

This reveals at what distance ($3.43 * 10^{16}$ cm) we begin to see deviations from spherical uniformity for IRAS 03206+6521 and the rate of change of uniformity over distance. Since locations farther out are believed to have been created earlier in time, this becomes a way to map uniformity over time. This distance and uniformity rate are starting points for three-dimensional non-uniform models. Models can inject non-uniformity at this distance to see if these stars evolve into the variety of planetary nebulae observed.

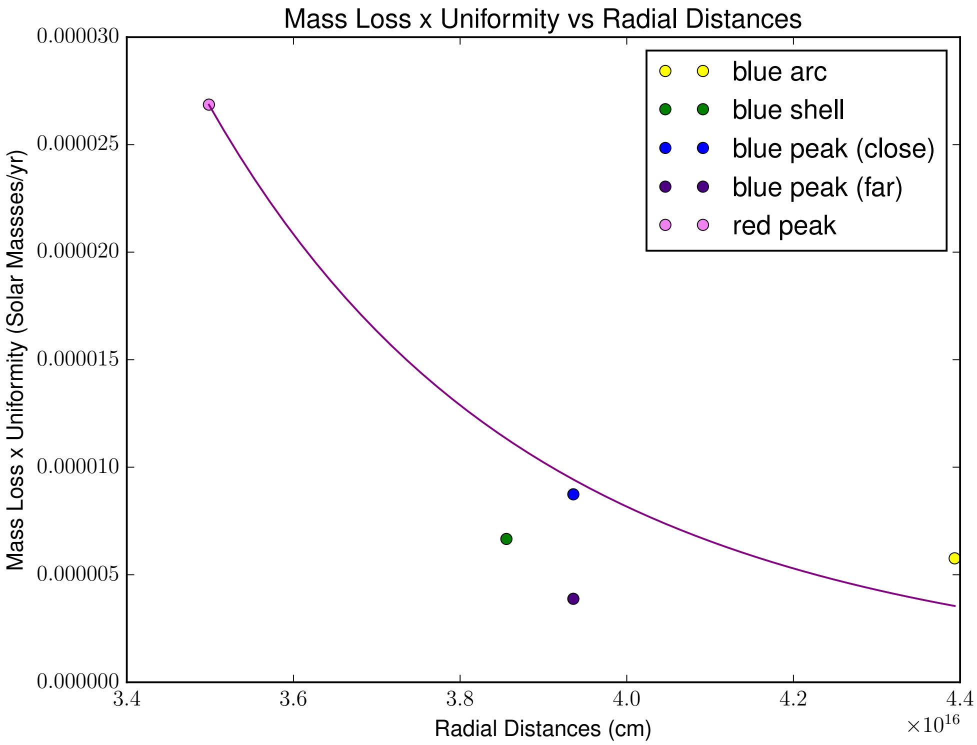

Figure 5.29 Using Netzer's mass loss estimates we weighted them by the uniformity we calculated through different layers in the OH maser shell. The points were weighted according to their detection Gaussian strength above the noise. The regions in the legend are data points from specific regions in the OH maser shell. In the regions where we find the peak of the blue-shifted spectral line we found 2 different maser shells at different radial locations and denote them "close" and "far" with respect to the center of the image.

Netzer & Knapp (1987) developed equations for mass loss rates from a spherically uniform model. Recall Netzer assumes a n_H/n_{OH} ratio. We used his equation adapted to our type of star to calculate the mass loss rates for several locations in the OH maser shell. To account for the uniformity we observed in the OH maser shell, we multiplied the mass loss rates from Netzer's equation suited for our source by the uniformity we measured. When we factor in the uniformity, the relationship goes from mass loss rates linearly increasing with radial distance (Netzer), to mass loss rates decreasing with radial distance, with a power law relation eq. (5.3). The points were weighted according to their detected Gaussian strength above the noise. From this equation, picking the largest mass loss rate given our radial distances and uniformity measurements, we get a mass loss rate of 2.69*10^{-5} $M_\odot$/yr, which is less than the amount Netzer's equations would predict (3.84$*$$10^{-5}$ $M_\odot$/yr). This comes from a piece of a shell that is 85% uniform. Our measurement is understandably less because we are weighting the uniformity and detecting a significant lack thereof. We also are using the distance on the near side of the shell, which will produce a smaller mass loss rate. This location happens to have a uniformity measurement 85% that equates best to Netzer's spherically uniform assumptions. Measuring mass loss on the near side of the shell may, in fact, be a better indicator of the more recent mass loss rate, itself being affected more recently by the star's mass loss process. With this greater detail accounting for non-uniform mass loss, we believe this is yielding a better estimate of the current mass loss rates.

$$M_\odot/yr = 1.83 * r^{-8.89} \tag{5.3}$$

We similarly handled the thickness versus mass loss rate relationship (see Fig. 5.30). When we factor in the uniformity, the relationship goes from mass loss rates decreasing with thickness to mass loss rates increasing with thickness, a relationship that perhaps is more intuitive eq. (5.4). Where thickness (in 10^{16} cm) is represented by the letter t. The points were weighted according to their detected Gaussian strength above the noise. Since the details of the uniformity of the mass loss processes are coming into play, the models are changing and we are better understanding our measurements.

$$M_\odot/yr = 0.000467 * t^{1.17} \tag{5.4}$$

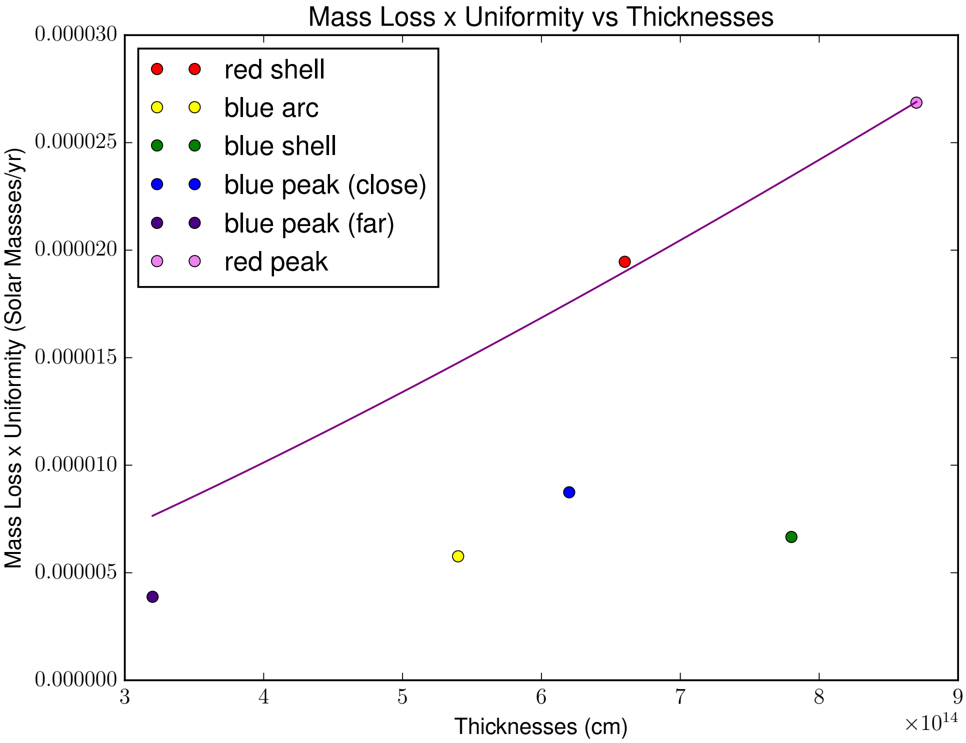

Figure 5.30 Using Netzer's mass loss estimates we weighted them by the uniformity we calculated through different layers in the OH maser shell and compared them to shell thickness. The points were weighted according to their detection Gaussian strength above the noise. The regions in the legend are data points from specific regions in the OH maser shell. In the regions where we find the peak of the blue-shifted spectral line, we found 2 different maser shells at different radial locations and denote them "close" and "far" with respect to the center of the image.

5.5 Dust Factor

The dust factor has been used by scientists in the past to determine the comparative amount of dust around a star. Traditionally, scientists look for reduced fluxes at higher frequencies to indicate a higher amount of dust, because dust preferentially scatters at higher frequencies. We determined dust factors by dividing the IRAS infrared 25-micron flux by the IRAS 12-micron flux equating larger dust factor ratios to being a stronger indicator of dustier shells. The Lewis chronology sequence predicts that a high concentration of dust surrounding OH/IR stars indicates larger and denser gaseous shells which indicate advanced age (Lewis 1989). We chose sources on this claim, attempting to select targets with large, thick maser shells. For two sources we found indicators of advanced age being that the 1612 MHz peaks are diminishing. In one source we found a large extended circumstellar envelope, a large mass loss rate, and a lack of H_2O masers all being late age indicators. So the dust factor produced two targets showing advanced age, and thus we support Lewis' predictions. Large amounts of dust are likely in the envelope due to a high mass loss rate.

5.6 Python Program

I developed a new python program for analyzing data because there was not a well-known tool to analyze circular or spherical uniformity of square images with square pixels. Other programs that were available involve analyzing objects as a whole, rather than being able to observe them in sections. Most importantly, these other programs are completely unable to handle data about an object if it is composed of rings. I had to create a size value (called a bin size) for space in between concentric rings to quantify specific ranges of radii within an observed circle to be observed as separate objects. In other words, this program was able to break the data up into layers like an onion, with the bin size representing the thickness of that layer and distinguishing it from each subsequent inner layer. This allows for super fine ring slices of the map, which gives extra accuracy when mapping energy density within the figure. These data were almost completely unobservable when reduced using traditional programs, but are clearly visible using this method. This is also the only program that is able to create a histogram depicting the flux of energy within each concentric circle. Then a Gaussian curve could be fit to the peaks of energy flux, with peaks representing the radial location, and width representing the thickness of a maser shell. It is a tool created to help observers measure circular or ring uniformities in objects from a distance.

In order to create this program, I had to give the user the ability to set lots of parameters to easily control how the data sets are handled. One such parameter, known as bin size, controlled the thickness of my circular cuts to measure an area to sample that would produce average intensity per area. Through controlling this I found the bin sizes of even 1 and 2 worked as well as 7, and thus allowed me to work with smaller bin sizes to determine measurements of mass loss and uniformity with higher spatial resolution. I also gave the program control to “zoom” in on special features, by allowing sectional pieces to be taken as the input. It produced the uniformity values I hoped for in this study and allowed great clarity.

Other projects could adapt this code to analyze different types of off-center circular uniformities, like those in planetary nebulae or supernova remnants. It could also be adapted to measure the uniformities of contour lines by building in specific contour values to search for and measure. To use it for this application, in the code where the energy flux histograms are fit with Gaussian curves over a particular angular range, one would just mark a particular contour value and search for it and return its radial value, instead of returning the peak’s radial distance. The full program of ∼824 lines can be found at https://github.com/dfelli/uniformity_analysis

Chapter 6

Conclusion

OH/IR stars are unique stars in a very late stage of evolution. Their large circumstellar envelope is filled with complex evolving structures. Once these envelopes are better understood, the general evolution of Asymptotic Giant Branch stars to planetary nebulae can be better modeled, developing a better link to understanding chemical evolution.

We, unfortunately, were only able to analyze one source in great detail because two of the sources couldn't be analyzed due to bad data and the others lacked maser detections at 1612 MHz and other OH transitions (0.1 mJy sensitivity). If we had detected masers at other OH transitions perhaps we could have seen some morphology to show how the various maser shells compete. We were limited in choosing targets that were close enough to resolve structure. We also wanted targets that showed they were well advanced in age (lots of dust in their envelopes). With this criteria, we sampled a group of likely stars that were past the stage where strong H_2O masers are normally seen. If we had observed H_2O masers our model could have extended across a larger portion of the circumstellar envelope. We suspect that in the sources where we didn't detect OH masers, those sources have evolved past the OH maser phase. Thirty years ago these sources had OH masers detected at single dish resolution.

IRAS 03206+6521, an OH/IR star, has many indicators that it was at a very late stage of evolution. These include:

1. The detection of the diminishing 1612 MHz OH maser line (especially the red-shifted peak)
2. The lack of water maser detection
3. The high dust factor (25-micron/12-micron flux)
4. The large OH maser shell extending out to $4.39*10^{16}$ cm (this dissertation)
5. The large mass loss rate (Netzer equation $3.84*10^{-5}$ $M_{\odot}$/yr) (this dissertation's adaptation of Netzer's equation adding uniformity $2.69*10^{-5}$ $M_{\odot}$/yr)
6. An increasing mass loss rate radially closer to the star (this dissertation) indicating mass loss increases in time.

These factors along with its proximity (2.4 kpc) make it a great source for studying maser shell structure. Measurements at six locations in the OH maser shell regions produced radial distances, thicknesses, uniformities, and mass loss rates. This source showed the following relationships:

1. Shell uniformity decreases with radial distance eq. (5.2)
2. Shell thickness decreases with radial distance eq. (6.1)

$$t = 1.64 * r^{-2.3} \tag{6.1}$$

3. When mass loss rates derived from Netzer's equation are scaled to uniformity (this dissertation) they show that the higher mass loss rates correlate to thicker (t - 10^{16} cm) shells eq. (6.2).

$$M_{\odot}/yr = 0.089 * t^{1.29} \tag{6.2}$$

The key findings from our high-resolution observations are these aforementioned relationships which we used to estimate the physical location ($3.43{*}10^{16}$ cm) of where the circumstellar envelope began to show non-uniformity. Models (which usually assume spherical uniformity) now have a location and rate at which to inject non-uniformity in shell expansion. We suspect this alone can fill a large gap in how a spherical star can evolve to form the large variety of planetary nebulae observed in the sky. Our work supports two theories of what might be the major cause or shared cause of this non-uniformity.

First, the non-uniformity may be due to the environment that the circumstellar envelopes have to push against as they expand. Planetary nebulae have been observed in various environments: where the distribution of stars is not uniform, where supernova explosions affect and compress portions of the interstellar medium, and where clouds clump, changing the density in the region (see Fig. 1.3). Since our estimate for the start of the non-uniformity is at $3.43{*}10^{16}$ cm, a rather large distance, the environment may very well strongly affect the mass loss.

Second, magnetic fields may be the cause of the non-uniformity. The location at which the non-uniformity appears to take root is very close to the region where H_2O dissociates into the OH ion ($3.43{*}10^{16}$ cm by a small extrapolation). Magnetic fields accelerate charged particles in a moving medium, which would apply to this environment. Magnetic field strengths of 0.0698 +/- 0.034 μTesla were measured by our spectral lines, exhibiting Zeeman Splitting of hyperfine structure. This measurement is on the low side 10 to 100 times less) as far as magnetic field measurements normally go in these stars (Wolak et al. 2012).

Truly each environment can be unique, but non-spherical mass loss models will be better able to accurately predict the specific types of planetary nebulae that we see today. This can provide a useful tool for determining the types of stars and environments (be it magnetic fields or external structure).

For future work we expect to: build and test non-uniform mass loss models; determine if magnetic field, equatorial wind, or external structure (or what combination of these factors) is the best means to explain the high-resolution data; observe stars at different stages of evolution where maser could potentially reveal more structural detail; adapt the python code to explore taking in several images to measure 3-D structure of maser shells; adapt the python code to analyze other kinds of astronomical phenomenon; measure life spans of the circumstellar shells and predict life spans of asymptotic giant branch stages; re-observe two sources (that we observed at non-ideal times) that show promise of useful structure; and use the Very Large Array to detect spectral line strengths in nearby OH/IR stars.

We trust that this work will significantly improve mass loss readings and predictions for asymptotic giant branch stars, as well as provide a means to analyze other types of astronomical objects.

Bibliography

Baud, B., & Habing, H. J. 1983, A&A, 127, 73

Baumann, M. K., Hopkins, W., Nolletti, L., & Soluri, M. 2007, Cosmos Images from Here to the edge of the Universel (London, UK: Duncan Baird Publishers)

Bowers, P. F., Johnston, K. J., & Spencer, J. H. 1983, ApJ, 274, 733

Decin, L., Hony, S., de Koter, A., Justtanont, K., Tielens, A. G. G. M., & Waters, L. B. F. M. 2006, A&A, 456, 549

Fong, D., Justtanont, K., Meixner, M., & Campbell, M. T. 2002, A&A, 396, 581

Gómez, Y. 2007, in IAU Symposium, Vol. 242, Astrophysical Masers and their Environments, ed. J. M. Chapman & W. A. Baan, 292–298

Habing, H. J., te Lintel Hekkert, P., & van der Veen, W. E. C. J. 1989, in IAU Symposium, Vol. 131, Planetary Nebulae, ed. S. Torres-Peimbert, 359–380

Herman, J., Baud, B., Habing, H. J., & Winnberg, A. 1985, A&A, 143, 122

Lewis, B. M. 1989, ApJ, 338, 234

Marshall, J. R., van Loon, J. T., Matsuura, M., Wood, P. R., Zijlstra, A. A., & Whitelock, P. A. 2004, MNRAS, 355, 1348

Mauron, N., & Huggins, P. J. 2006, A&A, 452, 257

Mauron, N., Huggins, P. J., & Cheung, C.-L. 2013, A&A, 551, A110

Migenes, V., Cohen, R. J., & Bowers, P. F. 1991, in BAAS, Vol. 23, Bulletin of the American Astronomical Society, 825

Neri, R., Kahane, C., Lucas, R., Bujarrabal, V., & Loup, C. 1998, A&AS, 130, 1

Netzer, N., & Knapp, G. R. 1987, ApJ, 323, 734

Ruiz-Velasco, A. E., Wittkowski, M., Wachter, A., Schröder, K.-P., & Driebe, T. 2011, A&A, 535, A100

Sanchez Contreras, C., Alcolea, J., Bujarrabal, V., & Neri, R. 1998, A&A, 337, 233

Schöier, F. L., Lindqvist, M., & Olofsson, H. 2005, A&A, 436, 633

Simis, Y., Icke, V., & Dominik, C. 2001, in Astrophysics and Space Science Library, Vol. 265, Astrophysics and Space Science Library, ed. R. Szczerba & S. K. Górny

Sugiyama, K., et al. 2017, PASJ, 69, 59

te Lintel Hekkert, P., Caswell, J. L., Habing, H. J., Haynes, R. F., Haynes, R. F., & Norris, R. P. 1991, A&AS, 90, 327

Vlemmings, W., van Langevelde, H. J., & Diamond, P. 2005, in Astronomical Society of the Pacific Conference Series, Vol. 340, Future Directions in High Resolution Astronomy, ed. J. Romney & M. Reid, 410

Vlemmings, W. H. T., Diamond, P. J., & van Langevelde, H. J. 2002, A&A, 394, 589

Wachter, A., Schröder, K.-P., Winters, J. M., Arndt, T. U., & Sedlmayr, E. 2002, A&A, 384, 452

Wolak, P., Szymczak, M., & Gérard, E. 2012, A&A, 537, A5

Zijlstra, A. A., Chapman, J. M., te Lintel Hekkert, P., Likkel, L., Comeron, F., Norris, R. P., Molster, F. J., & Cohen, R. J. 2001, MNRAS, 322, 280